

Multispectral Satellite Imagery Products for Fire Weather Applications

CURTIS J. SEAMAN,^a WILLIAM LINE,^b ROBERT ZIEL,^c JENNIFER JENKINS,^c CARL DIERKING,^d AND GREG HANSON^e

^a *Cooperative Institute for Research in the Atmosphere, Colorado State University, Fort Collins, Colorado*

^b *NOAA/Center for Satellite Applications and Research/Regional and Mesoscale Meteorology Branch, Fort Collins, Colorado*

^c *Bureau of Land Management, Alaska Interagency Coordination Center, Fort Wainwright, Alaska*

^d *Geographic Information Network of Alaska, University of Alaska Fairbanks, Fairbanks, Alaska*

^e *NOAA/National Weather Service, Boulder, Colorado*

(Manuscript received 12 September 2022, in final form 17 March 2023, accepted 22 March 2023)

ABSTRACT: Two multispectral satellite imagery products are presented that were developed for use within the fire management community. These products, which take the form of false color red–green–blue composites, were designed to aid fire detection and characterization, and for assessment of the environment surrounding a fire. The first, named the Fire Temperature RGB, uses spectral channels near 1.6, 2.2, and 3.9 μm for fire detection and rapid assessment of the range of fire intensity through intuitive coloration. The second, named the Day Fire RGB, uses spectral channels near 0.64, 0.86, and 3.9 μm for rapid scene assessment. The 0.64 μm channel provides information on smoke, the 0.86 μm channel provides information on vegetation health and burn scars, and the 3.9 μm channel provides active fire detections. Examples of these red–green–blue composite images developed from observations collected by three operational satellite imagers (VIIRS on the polar-orbiting platform and the Advanced Baseline Imager and Advanced Himawari Imager on the geostationary platform) demonstrate that both red–green–blue composites are useful for fire detection and contain valuable information that is not present within operational fire detection algorithms. In particular, it is shown that Fire Temperature RGB and Day Fire RGB images from VIIRS have similar utility for fire detection as the operational VIIRS Active Fire products, with the added benefit that the imagery provides context for more than just the fires themselves.

SIGNIFICANCE STATEMENT: The current generation of operational polar-orbiting weather satellites that began with the launch of *Suomi NPP* offers new capabilities with regard to fire detection and monitoring. In particular, false color red–green–blue composite imagery is now being used by fire managers, incident meteorologists, and others in the fire management community to visualize a fire's behavior and the context in which it occurs. This paper outlines two of these red–green–blue composites that have gained widespread use throughout the U.S. National Weather Service and the Alaska Fire Service. These red–green–blue composites have been applied to the current generation of geostationary and polar-orbiting satellites to great effect and have changed how incident management teams respond to wildland fires.

KEYWORDS: Algorithms; Geographic information systems (GIS); Satellite observations; Decision support; Forest fires

1. Introduction

Satellites are an important resource for the detection and monitoring of active wildland fires globally, particularly in remote locations where it is impractical to station human observers. The use of satellites for active fire detection and characterization began with the launch of the first Advanced Very High Resolution Radiometer (AVHRR) in 1979 (Dozier 1981; Matson and Dozier 1981; Flannigan and Vonder Haar 1986). These early studies demonstrated the value of spectral bands in the atmospheric window between 3.5 and 4.0 μm for

the detection of subpixel-sized heat sources. These methods have since been applied to a variety of low-Earth-orbiting (LEO) and geostationary (GEO) satellites (Prins and Menzel 1994; Weaver et al. 1995, 2004; Skrbek and Lorenz 1998; Giglio et al. 2003; Roberts et al. 2005; Ichoku et al. 2012).

The fire detection algorithm developed for the Moderate Resolution Imaging Spectroradiometer (MODIS; Giglio et al. 2003, 2016) has formed the basis of the Active Fire products that are now produced operationally from Visible Infrared Imaging Radiometer Suite (VIIRS) observations (Csiszar et al. 2014; Schroeder et al. 2014). The current operational fire detection algorithm for the Advanced Baseline Imager (ABI) on the GEO satellite platform (Schmidt et al. 2012; Li et al. 2020) is based on the Wildfire-Automated Biomass Burning Algorithm (WFABBA; Prins and Menzel 1994). These fire detection products compare brightness temperatures observed in the 3.5–4.0 μm atmospheric window and the 10–11 μm atmospheric window to identify subpixel-sized heat sources and use additional information provided by other spectral bands to screen for clouds. Quantitative estimates of fire intensity included in the fire detection products for MODIS, VIIRS, and

Denotes content that is immediately available upon publication as open access.

Supplemental information related to this paper is available at the Journals Online website: <https://doi.org/10.1175/JTECH-D-22-0107.s1>.

Corresponding author: Curtis Seaman, curtis.seaman@colostate.edu

DOI: 10.1175/JTECH-D-22-0107.1

© 2023 American Meteorological Society. For information regarding reuse of this content and general copyright information, consult the [AMS Copyright Policy](#) (www.ametsoc.org/PUBSReuseLicenses).

ABI are based on the fire radiative power (FRP) retrieval of [Wooster et al. \(2003\)](#) and use the 3.5–4.0 μm atmospheric window band alone.

While active fire retrievals, such as those referenced above, are vital for quantitative applications and supply critical information for assimilation into numerical models for fire and smoke forecasting (e.g., [Ahmadov et al. 2017](#)), they are, by design, “fire-centric”—focusing entirely on the fires themselves, and ignoring the full context of the scene that the imagery from the satellite provides. Fire managers in the field require more information than the active fire detections alone ([Johnston et al. 2020](#)). For example, what is the fire’s extent? What is the condition of fuels in the vicinity of the fire? Are there geographic features nearby that would limit fire spread (e.g., bodies of water, bare ground, previous burn scars)? How much smoke is there and where is it headed? Current operational quantitative fire detection/retrieval products, such as the VIIRS Active Fire product or ABI Fire/Hot Spot Characterization product ([Schmidt et al. 2012](#)), cannot answer these questions. Additional information is required, often requiring additional data products that must be georeferenced to the location of the fire and displayed in a common framework. Merging disparate datasets into a common display framework in a low-bandwidth environment (i.e., on site at a wildland fire with limited Internet access) is currently a major challenge of the operational fire management community ([Delamere et al. 2021](#)). Of particular importance is presenting these data in a visually intuitive manner such that fire managers, who are often not remote sensing experts, can easily interpret the data in the context of other hazard and value information and convert the suite of information into impact-mitigating actions.

An alternative approach that has gained momentum within the fire management community in recent years ([Delamere et al. 2021](#); [Straka et al. 2021](#)) is to use the satellite imagery itself, combining information from multiple spectral bands that provide information on hotspots, vegetation health, clouds, and smoke in a single image. The overarching goal of this imagery-based approach is to provide useful information to the operational fire management community in such a manner as to allow an individual observer, who need not be a remote sensing expert, to discern easily both the location of the fire and the context in which it occurs. While image analysis is inherently qualitative, this approach provides for rapid assessment of the scene with minimal training, and if the color components are properly chosen, the imagery will provide valuable information not present in current active fire detection products. In addition, the quantitative fire products may easily be overlaid on the imagery with minimal additional computational cost.

The products presented here take the form of false color imagery products that combine observations from multiple spectral bands into a single image ([d’Entremont and Thomason 1987](#)). These false color images are composed of either individual spectral bands or combinations of bands placed in the red, green, and blue color components of the image, and are commonly referred to as RGB composites. In this way, the information from multiple spectral bands is related to color as

provided by the RGB color model. In this work, these RGB composites are created using the data from three optical imagers from the current generation of operational weather satellites: VIIRS on the LEO platform ([Hillger et al. 2013](#)) and ABI ([Schmit et al. 2017](#)) and the Advanced Himawari Imager (AHI; [Bessho et al. 2016](#)) from the GEO orbit. These imaging instruments offer new capabilities with regard to fire detection and monitoring and the imagery from these instruments is already being analyzed by the operational user community for this purpose. [Lindley et al. \(2016, 2019\)](#) demonstrate how near-real-time monitoring of single-channel 3.9 μm satellite imagery within the U.S. National Weather Service (NWS) operations is used to alert emergency managers of new fire starts and monitor fire behavior.

In the following sections, two false color RGB composites are presented that have been designed specifically to facilitate the detection and monitoring of fires and other subpixel hotspots through image analysis. The first, named the Fire Temperature RGB, uses information from the 1.6, 2.2, and 3.9 μm spectral bands to relate fire intensity with color in RGB space in an intuitive manner. The second, named the Day Fire RGB, uses information in 0.65, 0.86, and 3.9 μm spectral bands to create imagery with the appearance of the “Natural Color RGB” ([Lensky and Rosenfeld 2008](#)), yet is highly sensitive to subpixel hotspots. The Day Fire RGB provides information on vegetation health and smoke in addition to fires. Both RGB composites have the potential to serve as qualitative fire masks that supplement the information provided by quantitative fire detection products.

This paper is outlined as follows. [Section 2](#) discusses the general foundation of RGB composites and defines the Fire Temperature and Day Fire RGBs. [Section 3](#) provides examples of these RGB composites with a focus on operational use cases that highlight how these RGB composites might be used (or are currently being used) by the fire management and fire weather forecasting communities. [Section 4](#) discusses how these RGB composites compare to the operational VIIRS fire detection algorithm, and [section 5](#) provides a summary and conclusions.

2. Theoretical background

a. RGB composites

The concept of RGB composite imagery derives from the additive color model of the same name used by a wide variety of digital display systems and image file formats. The RGB color model may be traced back to late-nineteenth-century research on the sensitivity of the human eye to color ([von Helmholtz 1924](#)), and was standardized by the Commission Internationale de L’Eclairage (CIE), also known as the International Commission on Illumination, in 1931 ([Smith and Guild 1931](#)). In short, it was found that by varying amounts of red, green, and blue light emissions, a spectrum of colors may be produced that simulates the range of sensitivity of nondeficient human color vision. In modern applications, these red, green, and blue light emissions are quantized with 8-bit radiometric resolution for each of the three primary colors (24 bits total),

leading to $256^3 \approx 16.7$ million colors. In contrast, single-channel imagery is typically limited to 8 bits (256 colors), either in grayscale or through the application of a color table. The breadth of color offered by RGB composites is advantageous for the imagery analyst, as it has been shown that normal human vision is sensitive to approximately 10 million colors, yet only about 30 shades of gray (Judd and Wyszecki 1975; Sharma and Trussell 1997; Glover et al. 2011).

In addition to the wealth of color, RGB composites offer the ability to combine the information present in multiple spectral bands (or band differences) into a single image. If the components of the RGB composite are selected wisely, the resulting image will contain significantly more information than any image made from the individual components. The primary challenge is in the selection and scaling of the R, G, and B components to produce an image that is straightforward for the human analyst to interpret.

In general, RGB composites are made by scaling floating point data between defined maximum and minimum values, converting the result into 8-bit integer values through the use of a gamma correction, and setting these values as the red, green, and blue components of the resulting image (EUMETSAT 2009). This is represented mathematically in Eq. (1):

$$I_{R,G,B} = 0 \leq 255 \left(\frac{D_{R,G,B} - \min_{R,G,B}}{\max_{R,G,B} - \min_{R,G,B}} \right)^{1/\gamma_{R,G,B}} \leq 255. \quad (1)$$

Here, D is the input floating point data, which is normalized by scaling between predefined maximum (max) and minimum (min) values. The gamma correction γ may be used (for $\gamma \neq 1$) to provide a nonlinear response between the linear scaling and the resulting image component intensity (I), which is clipped between values of 0 and 255 and converted to 8-bit integer type. The R, G, and B subscripts refer to the red, green, and blue components of the image, respectively, which are defined separately. Users should be aware that some software display packages (such as that used by the NWS) and some meteorological organizations use a definition of gamma that is the reciprocal of that shown in Eq. (1).

b. Fire Temperature RGB

The theoretical basis for the Fire Temperature RGB lies in Wien’s displacement law. Wien’s law may be derived from Planck’s law, which defines the spectral emission of a blackbody as a function of temperature:

$$B = \frac{2hc^2}{\lambda^5 \left(\exp \left[\frac{hc}{\lambda kT} \right] - 1 \right)}. \quad (2)$$

In Eq. (2), B is the blackbody spectral radiance for a given wavelength λ , and temperature T , c is the speed of light, h is the Planck constant, and k is the Boltzmann constant. Examples of blackbody spectra for various temperatures are shown in Fig. 1. The wavelength of peak emission λ_{peak} may be found by locating where the derivative of (2) with respect to λ is equal to zero for a given T . This is Wien’s displacement law:

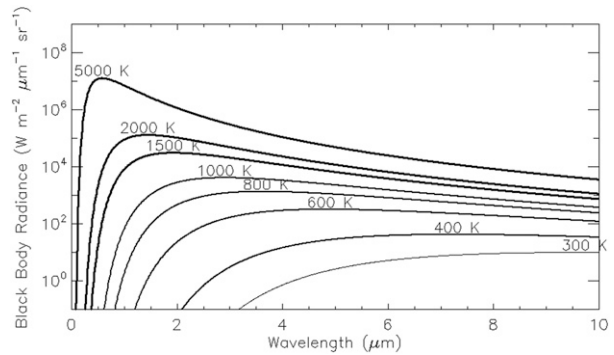


FIG. 1. Blackbody emission spectra for selected temperatures.

$$\lambda_{\text{peak}} = \frac{b}{T}. \quad (3)$$

Here, b is Wien’s displacement constant, approximately $2898 \mu\text{m K}$. Simply put, as the temperature of a blackbody increases, the peak of the emission spectrum is shifted to shorter wavelengths—a characteristic that is exploited by the Fire Temperature RGB.

Quantitative detection of fires at the resolution of contemporary meteorological satellite imagers, $O(0.1\text{--}4)$ km, requires a bispectral or multispectral approach (e.g., Dozier 1981; Giglio et al. 2003) to identify subpixel-sized hotspots, as the flaming portion of a wildland fire rarely fills an entire pixel so that full-field-of-view pyrometry assumptions do not apply (Elvidge et al. 2013). On spatial scales of 100 m or more, pixels containing active burning are typically a nonhomogeneous mixture of flaming, smoldering, and nonburnt components (Kaufman et al. 1998; Giglio and Kendall 2001). These bispectral techniques take advantage of the fact that channels in the $3.5\text{--}4.0 \mu\text{m}$ atmospheric window are more sensitive to subpixel-sized heat sources than channels in the $10\text{--}11 \mu\text{m}$ atmospheric window so a comparison between these channels is used to identify pixels containing active fires.

During the daylight hours, radiation observed by satellites in the $3.5\text{--}4.0 \mu\text{m}$ atmospheric window is composed of both direct emissions from the Earth–atmosphere system, as well as reflected solar radiation (Kidder et al. 2000). At longer wavelengths, direct emission dominates the signal, while at shorter wavelengths the reflection of solar radiation dominates. Figure 2 shows the solar irradiance spectra (Gueymard et al. 2002) along with reflectance spectra of varying surface types (Baldrige et al. 2009) and the spectral bands of several existing and near-future meteorological satellite imagers (WMO 2019). The “soil,” “snow,” and “vegetation” spectra shown in Fig. 2c are averages of the available soil and vegetation types and snow grain sizes included in the ASTER Spectral Library version 2.0 (Baldrige et al. 2009). While there is considerable variation in the reflectance spectra of specific vegetation species (Meerdink et al. 2019), the general trends discussed below are similar to those shown in Fig. 2c. Note also in Fig. 2b that different imaging instruments have different spectral characteristics (i.e., spectral width and central

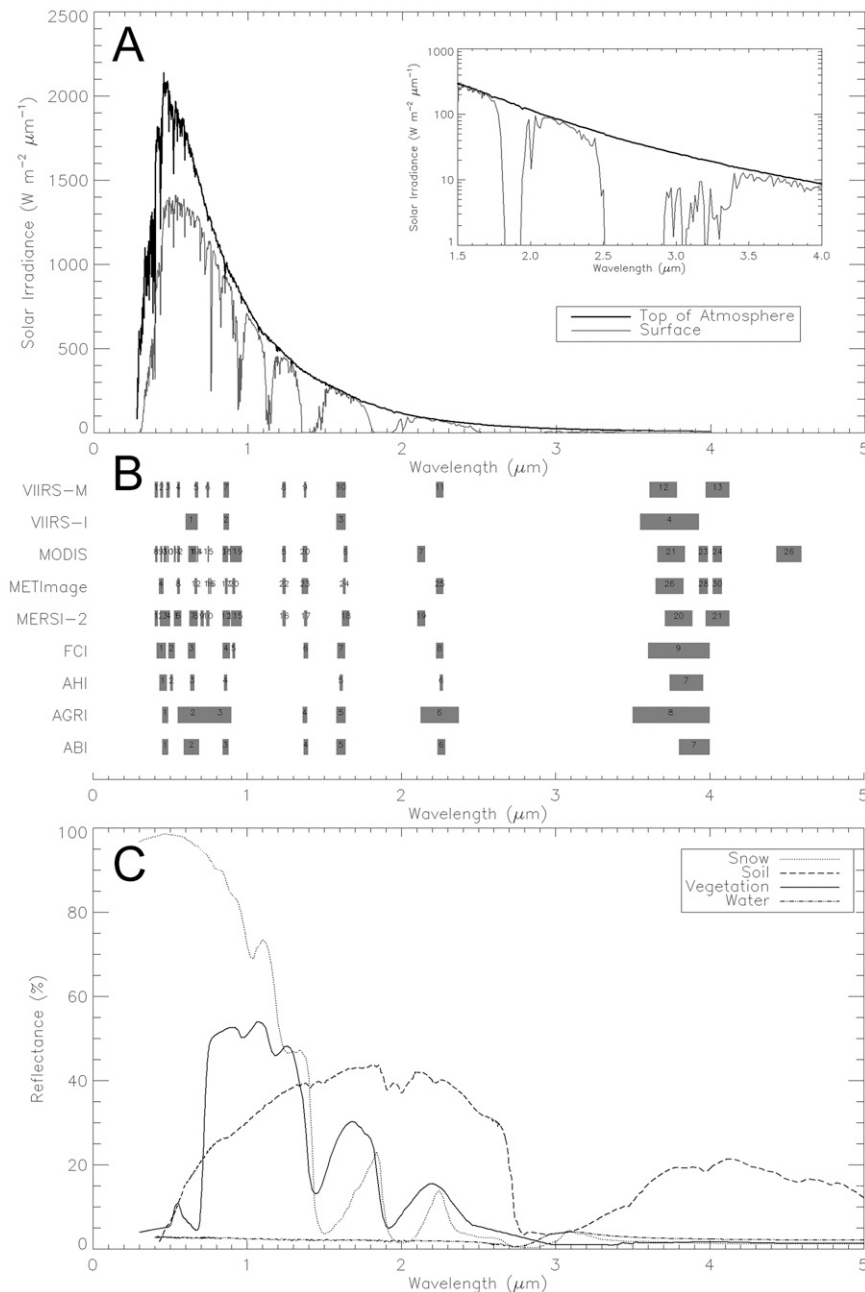


FIG. 2. (a) Solar irradiance spectra at the top of the atmosphere and the surface (from Gueymard et al. 2002). The inset is zoomed in on the region of interest for the Fire Temperature RGB and is plotted on a logarithmic scale. (b) Spectral channels of selected meteorological imagers capable of displaying the Fire Temperature RGB and Day Fire RGB. See appendix for acronym definitions. Note that to avoid overlap, the VIIRS Imagery (VIIRS-I) bands and Moderate-resolution (VIIRS-M) bands are plotted separately. (c) Reflectance spectra of selected surface types (from Baldridge et al. 2009).

wavelength) in these channels. For simplicity, all spectral channels that fall within the 1.5–1.8 μm atmospheric window will be referred to as 1.6 μm . Spectral channels in the 2.0–2.5 μm atmospheric window will be referred to as 2.2 μm and channels within the 3.5–4.0 μm atmospheric window will be referred to as 3.9 μm , regardless of central wavelength.

Of note in Fig. 2a are the 1.6 and 2.2 μm atmospheric windows highlighted in the inset. In this portion of the spectrum, the amount of incoming solar radiation increases with decreasing wavelength. In addition, peaks in the reflectance spectra of vegetation and soil are typically greater at 1.6 μm than at 2.2 μm (Fig. 2c). Therefore, the equivalent blackbody

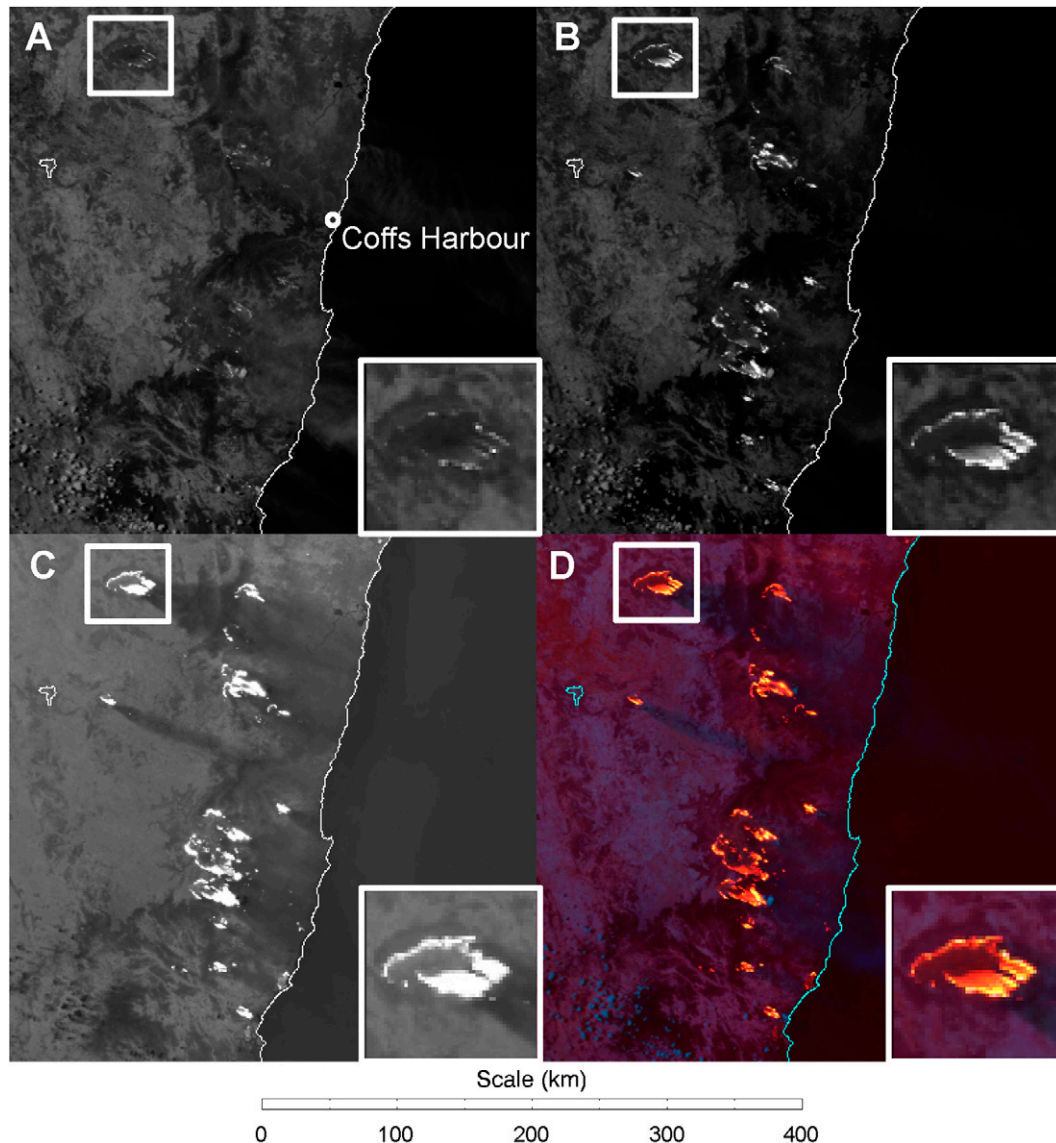


FIG. 3. SNPP VIIRS images of wildland fires in southeast Australia (0329 UTC 8 Nov 2019). (a) Channel M-10 ($1.61 \mu\text{m}$), (b) channel M-11 ($2.25 \mu\text{m}$), (c) channel M-13 ($4.0 \mu\text{m}$), and (d) Fire Temperature RGB. In each, the inset is zoomed in on the northwesternmost fire outlined. Note that the scale bar below the figure does not apply to the insets.

temperature of a fire must increase for the emitted radiation signal to be detected above the background of reflected solar radiation at these shorter wavelengths, as shown in Fig. 1. As such, while spectral bands near $3.9 \mu\text{m}$ have sensitivity to a wide range of fire temperatures and sizes, only a subset of fires will be intense and/or large enough to be detectable at $2.2 \mu\text{m}$, and only very intense and/or large fires will be detectable at $1.6 \mu\text{m}$. An example of this is shown in Fig. 3.

The Fire Temperature RGB uses these three spectral bands (1.6 , 2.2 , and $3.9 \mu\text{m}$) in a novel way to display fire intensity in a visually intuitive way. As shown in Fig. 3d, when the $1.6 \mu\text{m}$ channel is set as the blue component, the $2.2 \mu\text{m}$ channel as the green component and the $3.9 \mu\text{m}$ channel as the red

component of the image, hotspots from fires take on the visual appearance of flames that follow the spectral behavior of blackbody emitters. Relatively small, low intensity, or smoldering fires that are only apparent in the $3.9 \mu\text{m}$ channel will appear red. Hotspots of moderate size and/or intensity that are detectable in the $2.2 \mu\text{m}$ channel will also be detectable at $3.9 \mu\text{m}$ and will appear orange to yellow (i.e., have high values of I_R , moderate to high values of I_G , and low values of I_B), depending on intensity. Fires that are large and/or intense enough to be detected at $1.6 \mu\text{m}$ will contribute to high color intensity in all three bands and appear pale yellow to white. This is similar to the coloration of flames resulting from the combustion of woody fuels as a function of temperature, and

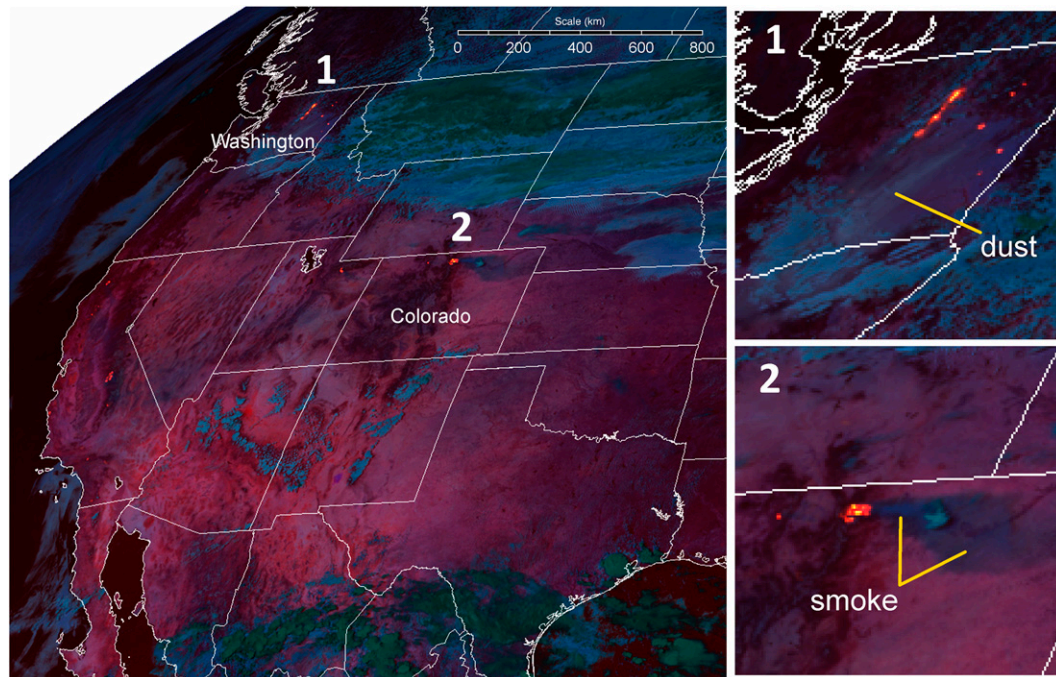


FIG. 4. (left) *GOES-16* ABI Fire Temperature RGB from 1956 UTC 7 Sep 2020. (top right) Inset 1 is zoomed in on fires over eastern Washington, and (bottom right) inset 2 is zoomed in on the fire in northern Colorado known as the Cameron Peak Fire.

this intuitive appearance facilitates user comprehension of fire behavior with minimal training. It should be noted that this is not a quantitative retrieval of the actual emissive temperature of the fire (e.g., Elvidge et al. 2013), but an image-based method for relating fire intensity to RGB coloration that provides the same information leveraged by the quantitative retrieval.

During sunlit conditions, this image-based approach provides additional information outside of the fire perimeter. Figure 4 shows a daylight example of the Fire Temperature RGB created from *GOES-16* ABI observations of the western contiguous United States (CONUS) when numerous large fires were observed across California, Washington, Colorado, and Utah. Geographical features are evident through the variation in color of the background land surface. In general, coniferous forests appear darker in color than deciduous forests, which, in turn, appear darker than croplands, grasslands, and desert areas (Baldrige et al. 2009; Meerdink et al. 2019). Cloud-top microphysical phase may be determined due to differences in reflectance between liquid cloud droplets and ice particles in the 1.6 and 2.2 μm components (Miller et al. 2014), which causes liquid-topped clouds to appear blue, while ice clouds appear dark green. While this RGB is relatively insensitive to

smoke and other aerosols, optically thick aerosol plumes may be apparent, as indicated in the insets of Fig. 4. Surface snow and ice, as well as bodies of water, are poorly reflective in all three image components and appear nearly black (except in regions of sun glint). At night, only direct emission sources (i.e., fires, gas flares, etc.) that are not obscured by clouds are apparent in the imagery, as non-emission sources require illumination by solar radiation to be apparent.

Table 1 shows the recommended recipe for the Fire Temperature RGB [i.e., the values of the constants required in Eq. (1)]. The use of calibrated radiance values as the input data source is recommended as ABI, AHI, and VIIRS all report valid radiance data at night in the required spectral bands. VIIRS does not report reflectance data for any of the solar reflective bands at night. At present, the Advanced Weather Interactive Processing System (AWIPS; Raytheon Intelligence and Space 2022), the primary data display system used by the NWS, is limited to display only reflectance values for reflective solar bands and brightness temperature for thermal infrared bands. Therefore, in order to facilitate a transition of this RGB into operational use by the NWS, a second recipe (Table 2) was developed based on 1.6 and 2.2 μm reflectance values and 3.9 μm brightness temperatures. This

TABLE 1. Values used in Eq. (1) that define the proposed standard definition of the Fire Temperature RGB.

Color	Input data (D)	Minimum (min)	Maximum (max)	Gamma (γ)
Red	3.9 μm radiance	0 $\text{W m}^{-2} \text{sr}^{-1} \mu\text{m}^{-1}$	3.5 $\text{W m}^{-2} \text{sr}^{-1} \mu\text{m}^{-1}$	1
Green	2.2 μm radiance	0 $\text{W m}^{-2} \text{sr}^{-1} \mu\text{m}^{-1}$	35 $\text{W m}^{-2} \text{sr}^{-1} \mu\text{m}^{-1}$	1
Blue	1.6 μm radiance	0 $\text{W m}^{-2} \text{sr}^{-1} \mu\text{m}^{-1}$	85 $\text{W m}^{-2} \text{sr}^{-1} \mu\text{m}^{-1}$	1

TABLE 2. Values used in Eq. (1) that define the Fire Temperature RGB for display in AWIPS.

Color	Input data (D)	Minimum (min)	Maximum (max)	Gamma (γ)
Red	3.9 μm brightness temperature	273 K	333 K	0.4
Green	2.2 μm reflectance	0%	100%	1
Blue	1.6 μm reflectance	0%	75%	1

alternative recipe was selected for its similarity in appearance to the radiance-based recipe in a wide variety of scenes around the globe. However, for hot, arid regions, the surface skin temperature may approach or exceed the 333 K maximum value used to scale the 3.9 μm channel in the AWIPS version (Jin and Dickinson 2010). In this case, the background land surface will appear sufficiently red to inhibit the detection of small fires by the average human analyst. It is recommended that users in these regions increase the max_R value to 343 K, as the surface skin temperature rarely approaches or exceeds this temperature except in landscapes devoid of vegetation (Mildrexler et al. 2011) where wildland fires are not expected to exist. Examples in this work that were produced outside of an operational environment were created using Table 1; however, users are encouraged to adjust either recipe as needed to account for differences in instrument characteristics (e.g., Berndt et al. 2018), display software and/or hardware limitations (e.g., Sharma and Trussell 1997), and/or personal sensitivity to color (e.g., Smith and Pokorny 1995).

c. Day Fire RGB

The basis of the Day Fire RGB derives from the Natural Color RGB developed by the European Organisation for the Exploitation of Meteorological Satellites (EUMETSAT) (Lensky and Rosenfeld 2008; EUMETSAT 2009). The Natural Color RGB was originally developed for the Spinning Enhanced Visible and Infrared Imager (SEVIRI) on the Meteosat Second Generation (MSG) satellites. As SEVIRI lacks the spectral channels needed to create True Color images (Miller et al. 2016), the Natural Color RGB was created as a suitable alternative. The recipe for the Natural Color RGB is shown in Table 3. In many scenes, the Natural Color RGB provides similar information as True Color, except that the use of the 1.6 μm channel allows for the discrimination of snow, ice, and ice clouds from liquid clouds. This is due to the low reflectance of snow and ice at 1.6 μm (Fig. 2c), while liquid clouds are highly reflective in all three channels. Thus, snow, ice, and ice clouds have a vivid cyan appearance (i.e., have high values of I_B and I_G , and low values of I_R), while liquid clouds are brighter in color and generally appear as a slightly cyan version of light gray. The use of the 0.86 μm channel, where healthy vegetation is highly reflective (Fig. 2c),

as the green component gives healthy vegetation a green appearance, while bare ground has a tan-to-brown appearance.

The Day Fire RGB replaces the 1.6 μm channel with the 3.9 μm channel as its red component. We recall here that the 1.6 μm channel is capable of detecting hotspots from only the most intense fires at the spatial resolution of most meteorological satellite imagers, while channels near 3.9 μm are sensitive to a much broader range of fire sizes and intensities. Figure 5 shows a comparison between a single-channel visible (0.64 μm) image, True Color RGB, Natural Color RGB, and Day Fire RGB applied to VIIRS for the same case shown in Fig. 3. The True Color RGB is a special case of RGB composite where the red-, green-, and blue-wavelength visible channels are combined as the R, G, and B components of the image and scaled to replicate normal human color vision (Miller et al. 2016; Broomhall et al. 2019; Miller et al. 2020). As shown in Fig. 5, the Day Fire RGB is much more sensitive to hotspots from fires than the standard Natural Color and True Color RGBs, yet still provides information on smoke and vegetation health. Hotspots from active fires, smoke and vegetation health are three key parameters required for effective active fire assessment.

Note that this RGB composite is intended for daylight-only use. Even for imagers that provide valid data at night in the solar reflective bands (e.g., ABI and AHI), the information content in the visible and vegetation-sensitive channels is lost without sunlight, reducing this RGB composite into a monochromatic (red) 3.9 μm image that is not optimized for nighttime use. Based on how this RGB composite is defined, information on clouds, smoke, and burn scars are lost in the absence of sunlight. In contrast, while the Fire Temperature RGB loses information on clouds and smoke at night, it will still provide similar information on fire intensity for sensors that provide these data at night.

A comparison between the Day Fire RGB and Fire Temperature RGB covering the transition from day to night is shown in the online supplemental materials as Video 1. This video was created from imagery produced from Himawari-8 AHI for a group of intense and rapidly expanding fires observed in southeast Australia on 7–8 November 2019 (same case as shown in Figs. 3 and 5). Due to the contributions of the shorter-wavelength channels, the Day Fire RGB is much more sensitive to smoke and other aerosols, while the Fire

TABLE 3. Values used in Eq. (1) that define the standard recipe of the Natural Color RGB (EUMETSAT 2009).

Color	Input data (D)	Minimum (min)	Maximum (max)	Gamma (γ)
Red	1.61 μm reflectance	0%	100%	1
Green	0.86 μm reflectance	0%	100%	1
Blue	0.64 μm reflectance	0%	100%	1

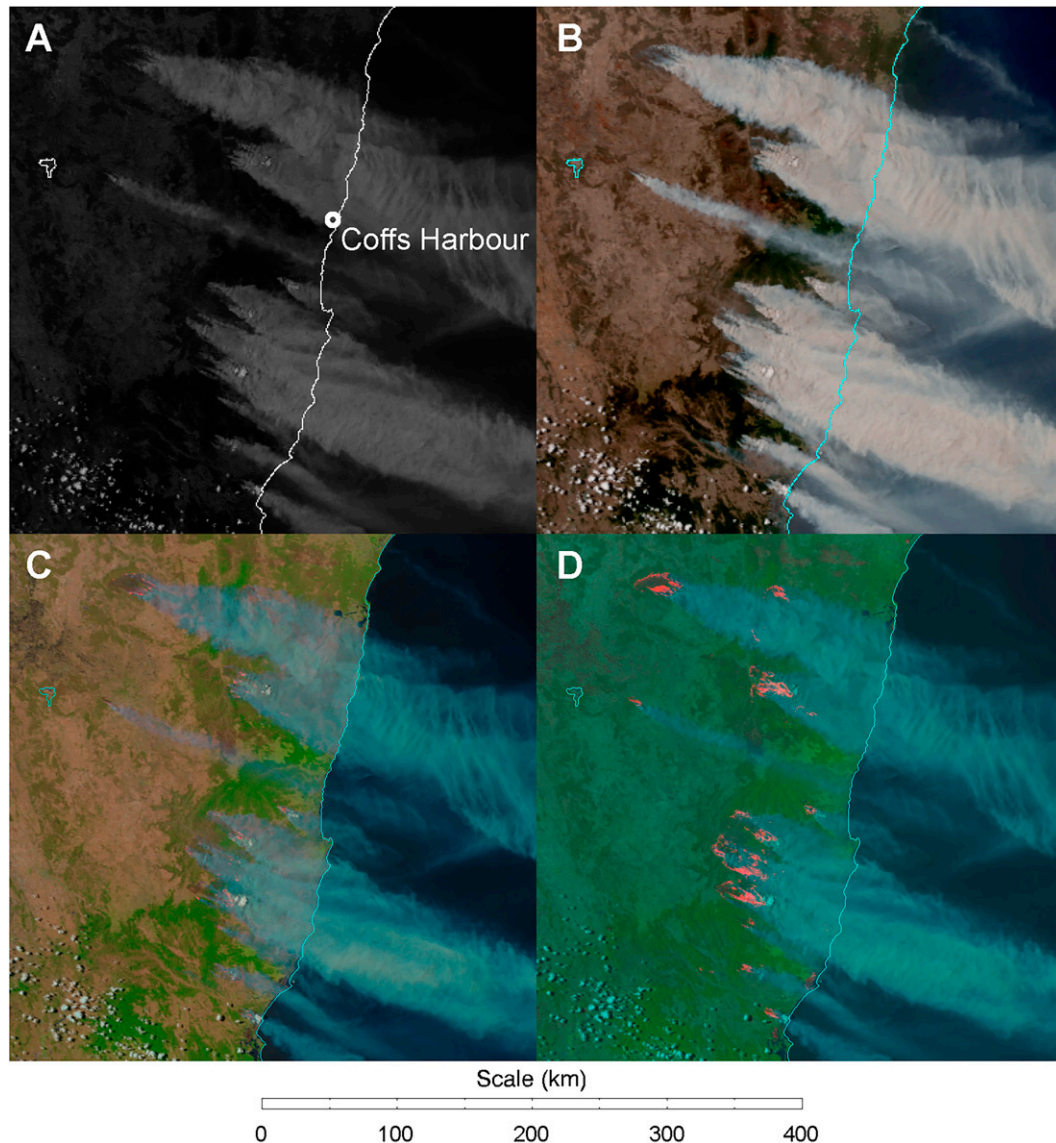


FIG. 5. *SNPP* VIIRS images of wildland fires in southeast Australia from the same case shown in Fig. 3. (a) High-resolution visible channel I-1 ($0.64 \mu\text{m}$), (b) True Color RGB, (c) Natural Color RGB, and (d) Day Fire RGB.

Temperature RGB provides information on fire intensity that is not present in the Day Fire RGB. This is evident when comparing Figs. 3 and 5.

The recipe for the Day Fire RGB is provided in Table 4. During the creation of this recipe, it was found that the utility of this RGB for fire detection is highly sensitive to scaling and selection of the red component input data and the characteristics of the satellite instrument used, particularly when used

for the detection of small fires. Figure 6 shows how the appearance of the Day Fire RGB changes in relationship to the input data and scaling for the $3.9 \mu\text{m}$ component. This figure shows *SNPP* VIIRS images of several fires in northern Nevada from 11 July 2017, the most prominent of which was named the Roosters Comb Fire. In each panel, the blue and green components were scaled as in Table 4, while the red component was created using scaled radiance values (Fig. 6a),

TABLE 4. Values used in Eq. (1) that define the proposed standard definition of the Day Fire RGB.

Color	Input data (D)	Minimum (min)	Maximum (max)	Gamma (γ)
Red	$3.9 \mu\text{m}$ reflectance	0%	50%	1
Green	$0.86 \mu\text{m}$ reflectance	0%	100%	2
Blue	$0.64 \mu\text{m}$ reflectance	0%	100%	2

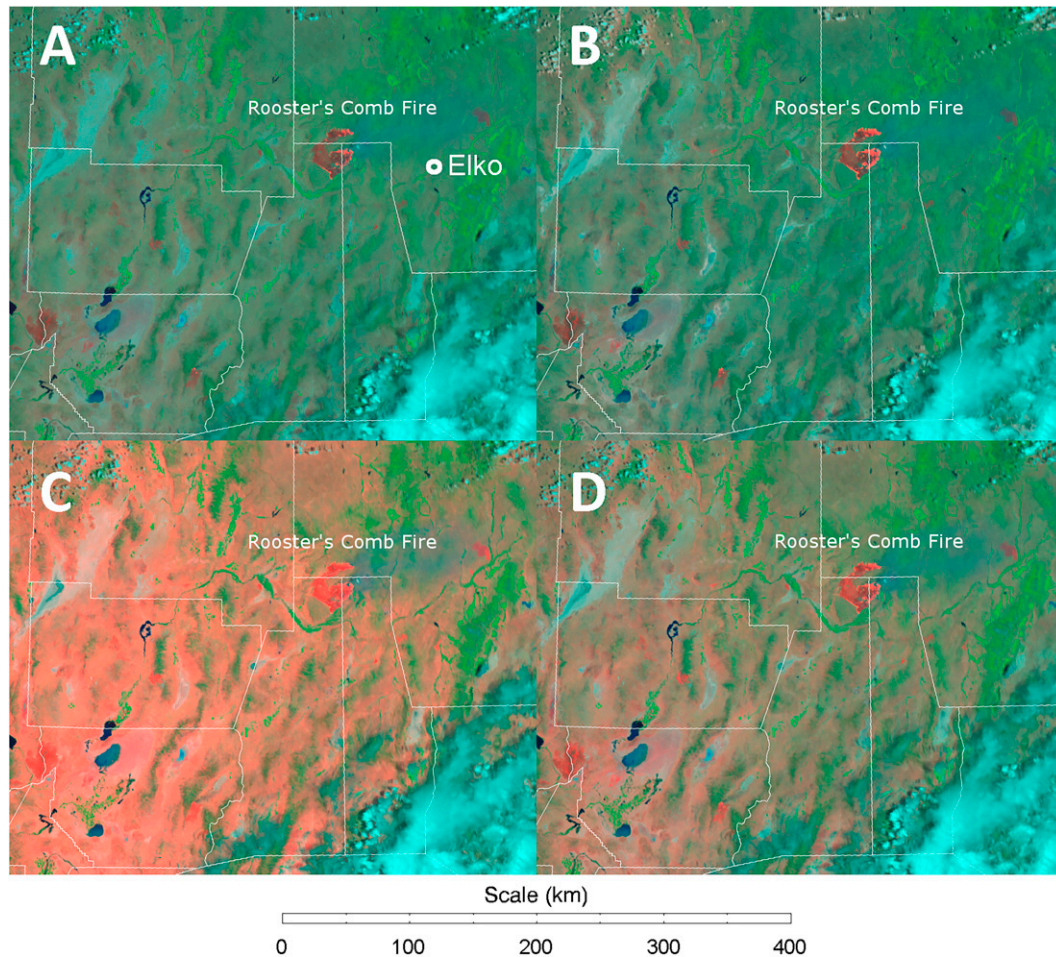


FIG. 6. Variations of the *SNPP* VIIRS Day Fire RGB from 2125 UTC 11 Jul 2017 for different $3.7 \mu\text{m}$ components: (a) using scaled radiance values ($0\text{--}3.5 \text{ W m}^{-2} \text{ sr}^{-1} \mu\text{m}^{-1}$) with a gamma value of 1, (b) using solar reflectance (0%–50%) with a gamma value of 1, (c) using scaled brightness temperatures (273–333 K) with a gamma value of 0.4, and (d) using scaled brightness temperatures (273–343 K) with a gamma value of 0.4. County boundaries of the state of Nevada are plotted for reference.

scaled solar reflectance (Fig. 6b), and scaled brightness temperatures (Figs. 6c,d). The retrieval of solar reflectance at $3.9 \mu\text{m}$ follows Kidder et al. (2000). The radiance version has reduced contrast relative to the other versions and reduced the detectability of smaller, less intense active fire pixels. Using similar brightness temperature scaling as in the AWIPS version of the Fire Temperature RGB (Fig. 6c) causes the background land surface to appear too red, which increases false alarms. In this case, burn scars and other nonburning, warm background surfaces appear red, similar to fires. Raising the value of max_R to 343 K mitigates this issue, to an extent, and makes the burn scars appear reddish-brown. However, the solar reflectance version (Fig. 6b) was determined to be the preferred appearance in a wide variety of cases. More of the pixels containing active fires appeared bright red relative to the radiance version with increased contrast against the background land surface, while the burn scars appear dark brown and distinctly different from the hotspots themselves. In addition, the

solar reflectance version is more useful in hot, arid regions, where most surface types are poorly reflective (Fig. 2c), yet may have high radiance (and, correspondingly, brightness temperature) due to their high skin temperature. However, it should be noted that there is also utility in having recently burned areas appear redder for perimeter mapping purposes. Overly dark burn scars may be difficult to distinguish from other dark surfaces. Users with adjustable display systems are encouraged to select the scaling that best fits their needs.

3. The utility of RGB imagery for fire monitoring and management

In this section, we will demonstrate the utility of the Fire Temperature RGB and the Day Fire RGB for fire detection, monitoring, and management. The following subsections discuss specific case studies where this imagery was used to support operational user communities and/or present other instances where

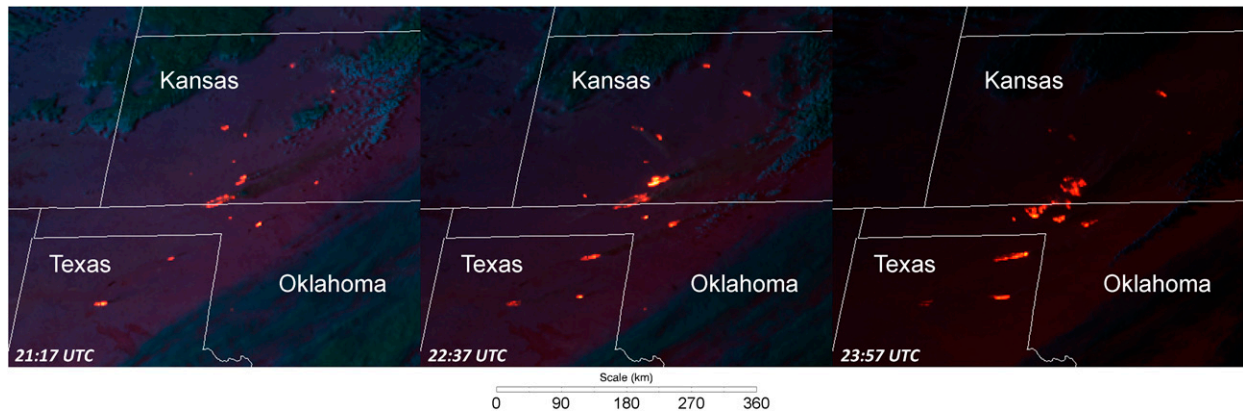


FIG. 7. A sequence of Fire Temperature RGB images from *GOES-16* ABI on 6 Mar 2017.

the imagery is expected to have a positive benefit on operations even if no operational use of the imagery was identified at the time.

While the specific case studies presented in this section come from within the boundaries of the United States, we note that the utility of these RGB composites as demonstrated here is not limited to the United States. The authors collectively have received feedback from users on every continent except Antarctica regarding the value of these RGB composites. However, it is not possible to include examples from each region on Earth in this paper. Sections 3a–c discuss case studies from the CONUS. Section 3d discusses more generally the use of these RGB composites within the Alaskan Fire Service.

a. Starbuck fire

On 6–7 March 2017, shortly after *GOES-16* ABI data began flowing to NWS Weather Forecast Offices (WFOs), and while the satellite was still undergoing postlaunch checkout activities at 89.5°W longitude, multiple grassland fires ignited across western Oklahoma, Kansas, and Texas. News reports estimated that these fires burned over 4500 km² in total and resulted in seven fatalities (CNN 2017). The largest of these fires, named the Starbuck Fire, ultimately burned approximately 3000 km² along the Oklahoma–Kansas border (Gabbert 2017).

Figure 7 shows a sequence of ABI Fire Temperature RGB images from 2117 to 2357 UTC 6 March 2017. A longer animation of this event covering the time period between 1602 UTC 6 March and 0532 UTC 7 March 2017 is included as Video 2 in the online supplemental materials. During the afternoon of 6 March, a cold front advanced to the south and east across western Kansas, reaching the Oklahoma and Texas Panhandle region in the early hours of 7 March. Ahead of this front, strong southwesterly winds pushed these fires rapidly toward the northeast. Note the southwest-to-northeast orientation of the fires at 2117 UTC in Fig. 7.

The Starbuck Fire was first apparent in the 1722 UTC ABI CONUS image. Analysis of subsequent images indicates that, between 1722 and 2122 UTC, the fire front advanced to the northeast at a speed between 2 and 4 m s⁻¹ during this 4-h

period, covering a total distance of approximately 48 km. During this time period, the advancing cold front is identified in the Fire Temperature RGB by a change in shading of the background land surface across western Kansas between a lighter maroon color ahead of the front to a darker purple color behind the front. This front reaches the Starbuck Fire by the 2252 UTC image, as evidenced by the sudden change in intensity of the hotspots (revealed through the change in color from red to yellow) along the fire's southern flank. At this time, the hotspot signal along the northern flank begins to disappear as the now northwesterly winds push that flank of the fire toward previously burned areas where the fuels have already been consumed. From that point, the northeastward movement of the fire is halted, and the fire front pushes to the southeast, nearly orthogonal to the original motion, at a speed between 1 and 2 m s⁻¹. Note the northwest-to-southeast orientation of the fires along the Kansas–Oklahoma border at 2357 UTC in Fig. 7. Nearly one by one, from north to south, the other hotspots visible in Video 2 exhibit a similar change in motion due to the passage of the cold front.

Rapid changes in fire motion and behavior are a significant mortality hazard for firefighters. In addition to the change in direction, many of the fires evident in Video 2 also exhibited a change in intensity coincident with the wind shift. Throughout this event, forecasters at NWS WFO in Dodge City, Kansas, were monitoring ABI imagery for new fire starts as well as monitoring the advancement of the cold front. This information was communicated to the incident management teams, who were able to adjust their evacuation strategies in preparation of the cold front passage and the resulting change in fire behavior. The Science and Operations Officer at the Dodge City WFO issued this statement (NWS Training Center 2017):

This was an excellent hands-on demonstration of the capability *GOES-16* provides to detect wildfires in real time. We were calling local officials and, in some cases, this was the first notification they had of these fires—even before they got 911 calls. Given how overwhelmed these rural counties were, they were very thankful for the heads up. They were able to begin planning evacuations before the fires turned due to the wind shift. I'm not sure how aware they would have been that day without us calling them directly.

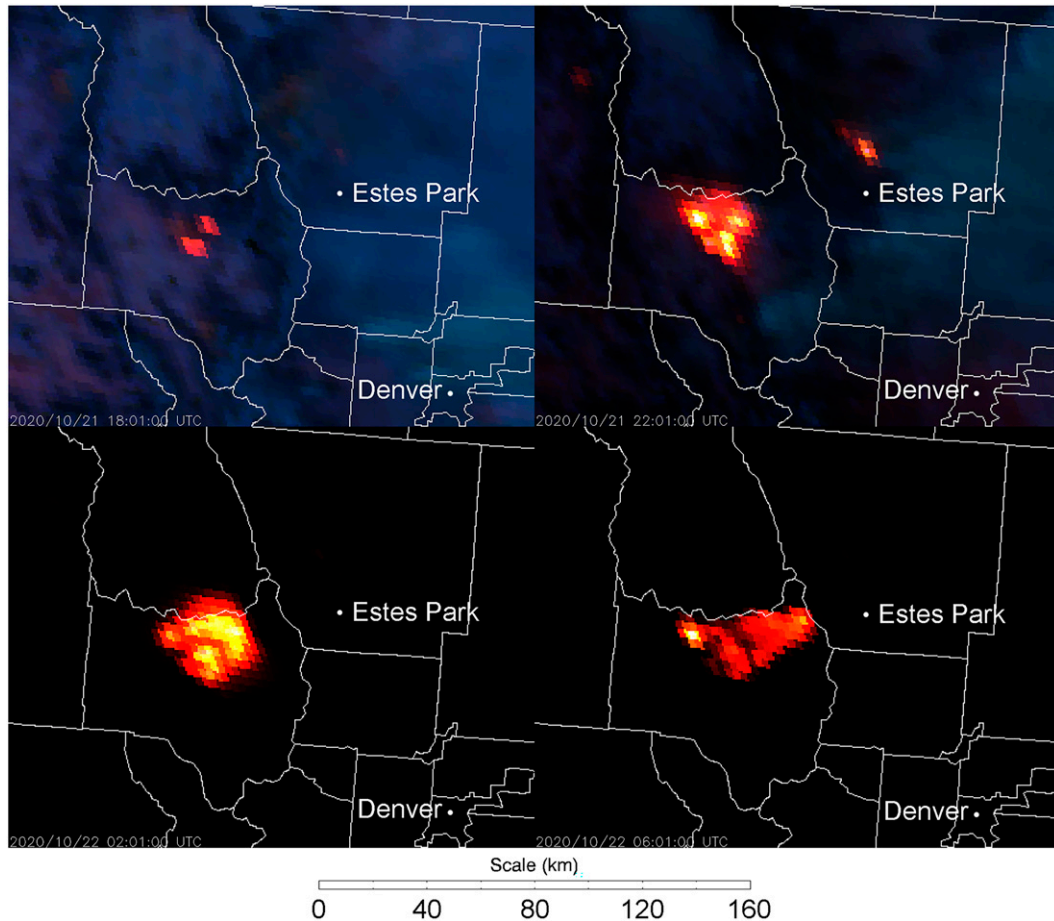


FIG. 8. Sequence of *GOES-16* ABI Fire Temperature RGB images of the East Troublesome Fire at 4-h intervals between 1800 UTC 21 Oct and 0600 UTC 22 Oct 2020. (upper right) The Cameron Peak Fire is also visible (2200 UTC 21 Oct 2020) as the isolated hotspot north of Estes Park.

Following the demonstration of this capability of ABI, the NWS requested the Fire Temperature RGB for their AWIPS display software for all WFOs within the ABI field of view. This led to the development of the RGB recipe provided in Table 2, as discussed in section 2c.

b. East Troublesome fire

The East Troublesome Fire was first reported on 14 October 2020, northeast of the town of Kremmling, Colorado. A combination of high winds, above normal temperatures, and low relative humidity values allowed the fire to spread quickly through an alpine forest marked by a high percentage of dead trees. During the period of 20–23 October 2020, the burned area increased by more than 400 km², with the largest single day increase of over 350 km² between the afternoons of 21–22 October (Colorado Encyclopedia 2023). Figure 8 shows a sequence of *GOES-16* ABI Fire Temperature RGB images during this period of rapid fire growth. One of the mesoscale sectors was located over this domain providing 1-min-temporal-resolution imagery throughout this period. An animation of the mesoscale sector imagery is provided in the online supplemental

materials as Video 3. Throughout this event, the NWS WFO in Boulder, Colorado (BOU), monitored the growth and intensity of the fire by viewing the Fire Temperature RGB in their AWIPS display software.

On the afternoon of 21 October 2020, NWS BOU meteorologists monitoring the East Troublesome Fire noted its intensification and rapid spread. This information was shared with the public via Twitter (NWS Boulder 2020a) at 1452 LT (2052 UTC). The tweet contained an animated GIF, captured from AWIPS, of the time lapse of Fire Temperature RGB imagery from 2011 to 2046 UTC 21 October 2020. Public safety was emphasized in subsequent social media posts, with a retweet of Grand County Sheriff evacuation orders.

Fire Temperature RGB imagery was included in a later tweet as another animated GIF from 2131 to 2221 UTC 21 October 2020, noting the explosive nature of the fire and a call to evacuate (NWS Boulder 2020b). The Fire Temperature RGB was used prominently in subsequent social media posts through the afternoon and evening to illustrate the rapid eastward spread of the fire and reinforce calls to evacuate. Between 0000 and 0700 UTC 22 October 2020, during a period

of high winds, the fire began a rapid run to the east, advancing toward the village of Grand Lake, on the southwestern boundary of Rocky Mountain National Park (RMNP) and the mountains along the Continental Divide that run through the park. This is included in Video 3 of the online supplemental materials.

With many peaks above 3500 m in elevation, the portion of the Continental Divide within RMNP is above the tree line, and was expected to act as a natural barrier to halt farther eastward progression of the fire front. Between 0900 and 1100 UTC, the eastward progression of the fire was halted by the vegetation-free mountains along the Continental Divide and this portion of the fire began to decrease in intensity. However, shortly after 1200 UTC, hot pixels became evident along or just on the east side of the Continental Divide at an elevation of 3700 m (Fig. 9). This analysis was complicated by the fact that ABI data are not corrected for parallax effects caused by the high terrain, which led to forecaster uncertainty of the location of the new fire start. At this elevation as viewed from *GOES-16* ABI, surface features in the imagery appear to be displaced ~ 5 km to the northwest of their actual position, which was known by forecasters given the peak's apparent location relative to the county boundary map. By accounting for parallax, NWS forecasters could conclude that the fire had indeed jumped the Continental Divide.

Once forecasters were reasonably certain of the validity of the data and mapping, calls were made to Larimer County Office of Emergency Management, Larimer County Dispatch/911 call center, and to RMNP dispatch. Visibility on the east side of the Continental Divide was limited by smoke from the fires for several days, and park officials had no prior indication that the fire had moved east of the Continental Divide until these calls. During these early conversations, the fire intensified with Fire Temperature RGB imagery indicating a rapid increase in heat and areal coverage (Figs. 9b,c). Response was mobilized: RMNP sent observers to confirm visually the fire's presence. The first call to officials was at 1307 UTC, and by 1600 UTC the fire was confirmed. Evacuation preparations for the west side of Estes Park, Colorado, the next town in the fire's path, were underway. RMNP closed and evacuated the park, with all hikers and visitors accounted for.

NWS BOU was the first to identify and provide notification of the fire's presence on the east side of the Continental Divide in RMNP, using the *GOES-16* Fire Temperature RGB imagery as the basis for that notification. Had that alert not happened, the fire would have continued to grow unnoticed for an additional unknown period. The time gained from the early satellite-based notification allowed for evacuations to take place, as well as firefighting measures to begin that would ultimately save the town of Estes Park.

c. Jack fire

Several large, high-impact wildland fires occurred in the Cascade Mountains of Oregon from 7 to 9 September 2020, ultimately burning more than 3900 km² of land, with at least 400 homes destroyed and 40 000 residents displaced by

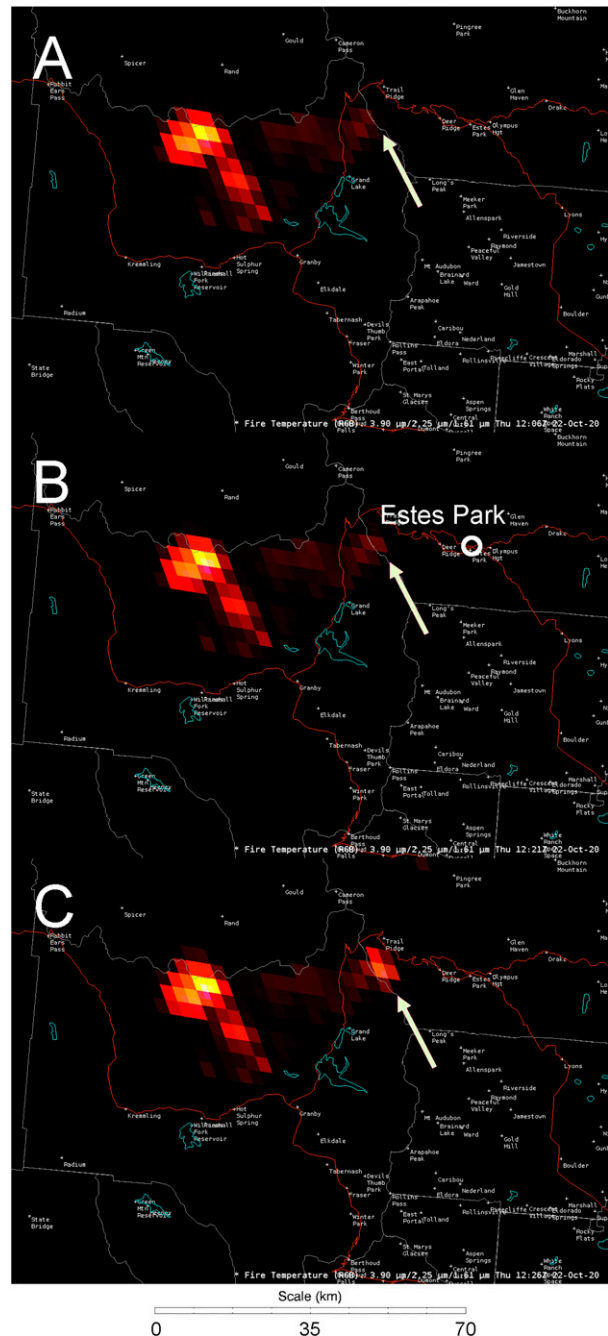


FIG. 9. *GOES-16* ABI Fire Temperature RGB images of the East Troublesome Fire: (a) 1206, (b) 1221, and (c) 1226 UTC 22 Oct 2020. In each panel, the arrow indicates the location of the Continental Divide in the area where the East Troublesome Fire crossed.

evacuation orders (Abatzoglou et al. 2021). Many of the burn scars resulting from these fires were clearly visible in the Day Fire RGB during the following summer (Fig. 10). One of these fires, named the Archie Creek Fire, burned more than 532 km² in the Umpqua National Forest northeast of Roseburg, Oregon. The postfire perimeter of the Archie Creek

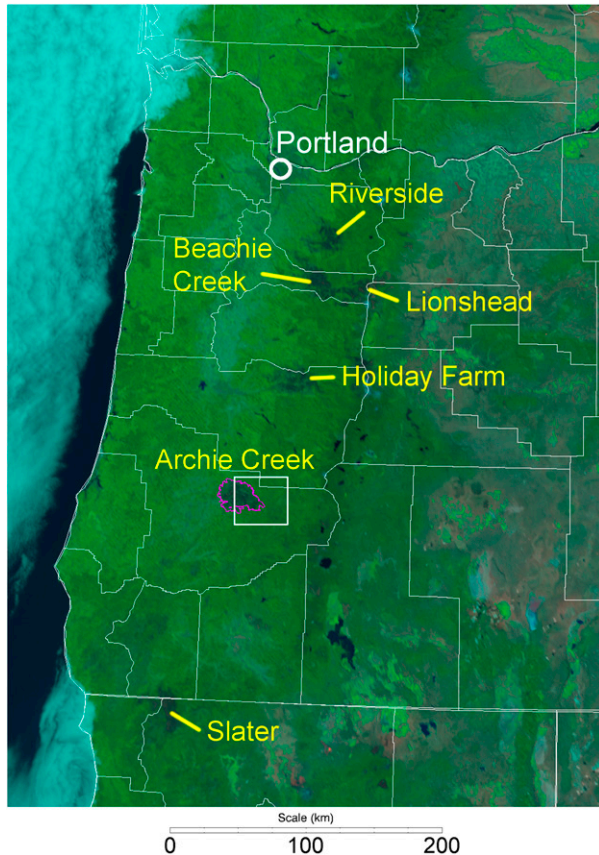


FIG. 10. SNPP VIIRS Day Fire RGB from 2006 UTC 5 Jul 2021 showing prominent burn scars resulting from the September 2020 fire event in western Oregon. The USFS postfire perimeter for the Archie Creek fire is highlighted in magenta. The white box indicates the approximate location of Fig. 11.

Fire from the U.S. Forest Service (USFS) National Fire Perimeter database (USFS 2021) is highlighted in Fig. 10.

On 5 July 2021, a fire was reported in Umpqua National Forest, near the eastern edge of the Archie Creek fire perimeter. This fire became known as the Jack Fire. Figure 11 shows a sequence of VIIRS Day Fire RGB images of the Jack Fire from 6 to 16 July 2021 taken from the afternoon overpasses from both SNPP and NOAA-20. A video animation of VIIRS Day Fire RGB images from the afternoon overpasses of 5–20 July 2021 is included in the online supplemental materials as Video 4. VIIRS imagery is shown here, as the Day Fire RGB is available with 375 m spatial resolution from all of the required bands (Fig. 2), as compared with nominal 2 km spatial resolution (at satellite subpoint) for the IR bands on ABI. The fire was first reported after the last VIIRS overpass on the afternoon of 5 July 2021 and was thus not visible in the imagery from that day. The first afternoon VIIRS overpass on 6 July occurred at 1948 UTC from SNPP. At that time, smoke from the Jack Fire was evident in the Day Fire RGB while the hotspot was not. Subsequent overpasses from SNPP and NOAA-20 on 6 July 2021 revealed the hotspot to be quickly expanding, primarily to the east, with some growth

to the north and south. With the Archie Creek burn scar to the west of the Jack Fire, growth to the west was limited.

During the course of the next two weeks, the Jack Fire exhibited growth to the south and west, around the southeastern edge of the Archie Creek burn scar (Fig. 11). Note that the fire did not cross the established perimeter of the Archie Creek Fire. The burn scar, which is clearly visible in the Day Fire RGB images, acted as an effective barrier to limit growth of the Jack Fire during this initial period when the most rapid growth occurred. Information on the presence of this burn scar is not available from either the ABI or the VIIRS quantitative fire detection products.

d. VIIRS RGB use within the Alaska Fire Service

The Alaska Fire Service (AFS) is a part of the U.S. Bureau of Land Management (BLM) responsible for providing fire suppression and management efforts in Alaska, along with USFS and the state of Alaska Department of Natural Resources (DNR) Division of Forestry and Fire Protection. AFS coordinates with a variety of federal, state, and local agencies to provide logistical and operational support related to fuels/fire management, aviation, planning, and fire ecology research through the Alaska Interagency Coordination Center (AICC).

Within Alaska prior to the launch of MODIS, the primary method for acquiring intelligence on new fire starts in remote regions of Alaska was through aircraft reconnaissance. These periodic flights required a considerable investment in resources and time, and were necessarily limited in areal coverage and temporal frequency. As a result, it could take several days to detect a new fire start. Use of aircraft reconnaissance during an active fire event may also be limited by the presence of hazardous weather and/or optically thick smoke.

Satellite detection of fires is not limited by pilot/aircraft availability and the VIIRS instruments on board the Joint Polar Satellite System (JPSS) constellation of satellites (Goldberg et al. 2013) provide complete coverage of Alaska multiple times per day. Due to the orbital characteristics of the JPSS satellites and Alaska's high-latitude location, VIIRS provides partial-to-near-complete coverage of the state approximately every 51 min between ~0000 and ~1800 LT (0900–0200 UTC) daily. The increased spatial resolution of the 3.9 μm bands on VIIRS over previous imagers (e.g., MODIS and AVHRR) and the low latency (~20 min or less) of direct broadcast data acquired from the Geographic Information Network of Alaska (GINA) at the University of Alaska Fairbanks have had a significant positive impact on operational fire management activities within Alaska.

The Day Fire RGB, in particular, is used to augment fire detections deriving from the VIIRS Active Fire products. A variety of users at AICC—including geographic information system (GIS) staff, Fire Management Officers, and Incident Management Team members—routinely inspect the imagery as it arrives to diagnose potential false alarms and hotspots not identified by the Active Fire products. Potential new fire starts are flagged and a risk–benefit analysis is performed to determine the allocation of resources for fire suppression/management efforts. Following the confident detection of a new fire based on this analysis, and weather permitting,

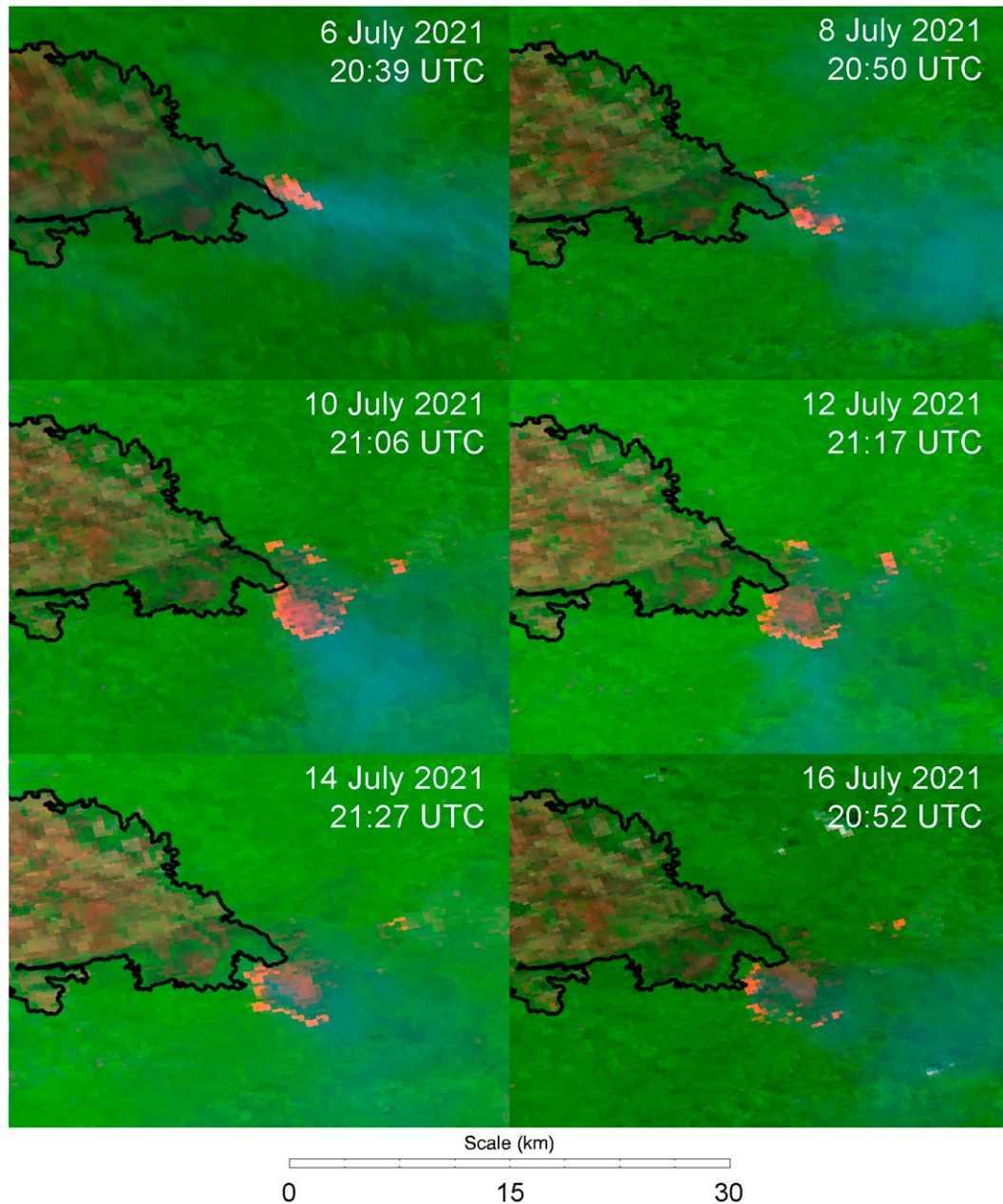


FIG. 11. Sequence of VIIRS Day Fire RGB images showing the growth of the Jack Fire (6–16 Jul 2021). For reference, the location of this fire is approximately 43.322°N, 122.686°W.

aircraft reconnaissance may be used to gather additional intelligence.

During an active fire event, the Day Fire RGB is used to monitor the movement of the active fire front, assess the size of the burned area and the mixture of burned and unburned vegetation within the fire perimeter, and estimate wind speed and direction from the visible smoke plume. The presence of clouds and optically thick smoke is also monitored for its impacts on hotspot detection and impacts on aviation activities related to fire management. Variations in the green coloration of vegetation in the RGB are used to discern regions

dominated by differing vegetation types that may alter fire behavior. In addition, Fire Temperature RGB images are used to monitor regions of increased fire activity and True Color RGB images are used as they provide increased sensitivity to smoke. These three RGB composites, as well as imagery made from the VIIRS 3.74 μm imagery-resolution channel (I-04), are displayed along with the VIIRS Active Fire detections and other ancillary data (e.g., ground-based lightning data, fire weather indices, administrative boundaries) within a web mapping service ([Alaska Fire Service 2022](#)).

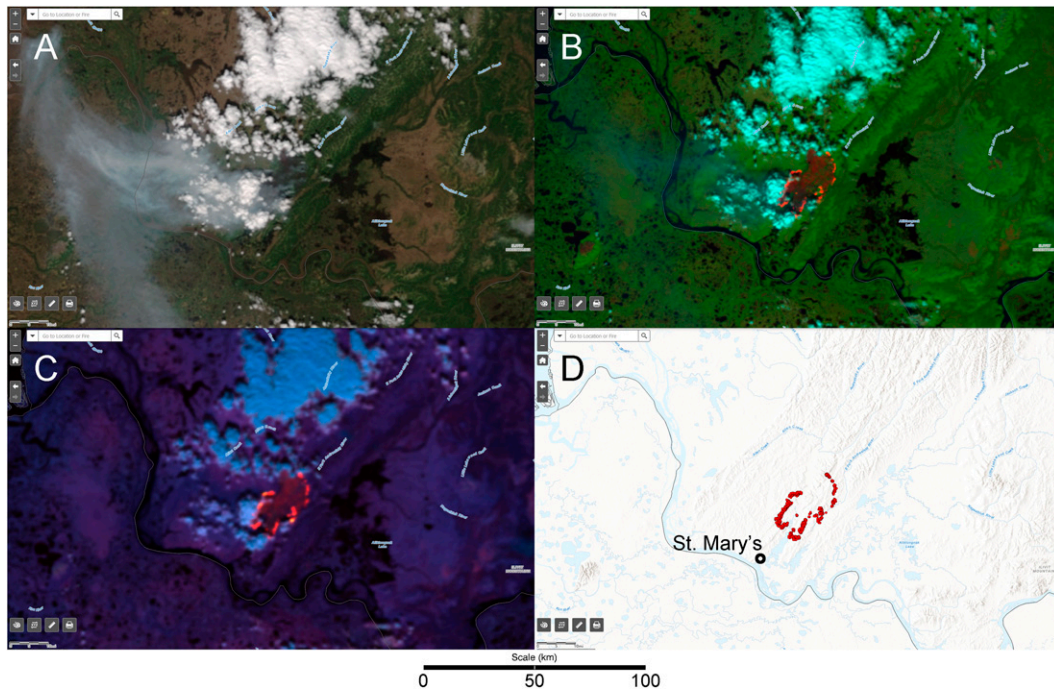


FIG. 12. VIIRS Imagery and I-band Active Fire data of the East Fork Fire near the village of Saint Mary's, Alaska, as observed on 9 Jun 2022. (a) *NOAA-20* VIIRS True Color image (2229 UTC), (b) *NOAA-20* VIIRS Day Fire RGB image (2229 UTC), (c) *NOAA-20* VIIRS Fire Temperature RGB image (2229 UTC), and (d) I-band Active Fire detections collected from all VIIRS overpasses on 9 Jun 2022 and displayed on the default background map used by AFS.

Figure 12 shows an example of the True Color RGB, Day Fire RGB, and Fire Temperature RGB from *NOAA-20* VIIRS for the East Fork Fire (2229 UTC 9 June 2022) as viewed on the AFS web mapping service. Also included are the VIIRS Active Fire detections, which are displayed as the aggregate of all VIIRS overpasses for the preceding 24 h period and plotted on the default base map (Fig. 12d). Note that each of these RGB composites contains significantly more information than the Active Fire detections alone. Through the duration of the East Fork Fire, it is estimated that VIIRS imagery was used from at least 262 overpasses and played a key role in helping AICC monitor fire activity throughout the landscape.

During an active fire season, users at AICC may be monitoring as many as 50 different fires simultaneously, ranging from small spot fires to large complexes. One of the advantages of the fire RGBs presented here is that, due to their intuitive display, fire detection and monitoring activities are no longer limited to remote sensing experts and image analysts. Users throughout the fire management enterprise, ranging from forecasters to incident response teams to Fire Management Officers make use of this imagery as part of their daily operations.

4. Comparison with quantitative retrievals

Due to the subjective nature of RGB composites, and differences in sensitivity to color between individuals, it is difficult to quantify the performance of these RGB composites

relative to the operational fire detection products produced from these imagers. Figure 13 shows the VIIRS Fire Temperature RGB and Day Fire RGB for a wildland fire in the vicinity of Tijuana, Mexico, from 8 December 2020. In each panel on the right, the fire detections and FRP retrievals from the 375-m-resolution VIIRS Active Fire product (Schroeder et al. 2014) are overlaid on the imagery. This example shows good qualitative agreement between the objective fire detection algorithm and the imagery. Note that the highest FRP retrievals align with the brightest pixels in the Fire Temperature RGB (produced at 750 m resolution), and that these are the pixels affected by saturation and radiance fold-over in the Day Fire RGB. Radiance fold-over occurs when the amount of radiation received by a detector greatly exceeds the detector's saturation limit, resulting in an artificially low radiance to be reported (Schroeder et al. 2014). These "fold-over" pixels do not appear red in the VIIRS Day Fire RGB. It may be noted that there are pixels that an analyst might determine as containing hotspots in the imagery where FRP was not retrieved in the Active Fire product. However, it is unclear if these are false alarms in the imagery, missed detections in the Active Fire product, or a combination of both. Further research with either ground or air support, or collocated observations from high-resolution satellite images (e.g., Landsat or Sentinel-2) would be needed to resolve these discrepancies.

It may be noted also from Fig. 13 that the VIIRS 375 m Active Fire product is able to detect fires and retrieve FRP in saturated pixels, while saturation artifacts impact the VIIRS

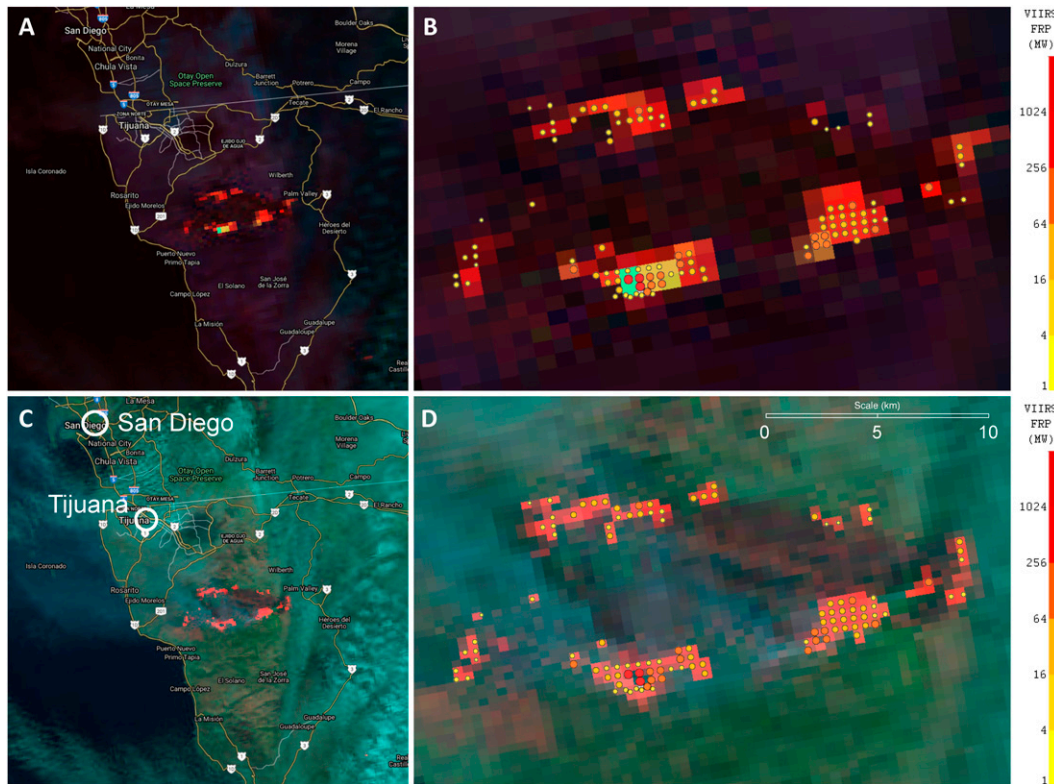


FIG. 13. NOAA-20 VIIRS images of a wildland fire near Tijuana, Mexico (2108 UTC 8 Dec 2020). (a) Fire Temperature RGB with map overlaid. (b) Fire Temperature RGB zoomed in on the fire with VIIRS 375 m Active Fire detections overlaid. (c) Day Fire RGB with map overlaid. (d) Day Fire RGB with VIIRS 375 m Active Fire detections overlaid. Active Fire detections are displayed as dots whose size and color are proportional to the retrieved FRP, as given by the scales on the right.

Day Fire RGB. Schroeder et al. (2014) have outlined the saturation mitigation strategy used in the Active Fire product, which is based on additional information from the 375-m-resolution $11.45 \mu\text{m}$ channel (I-05). At present, the AWIPS display system used by the NWS lacks the ability to perform such corrections in its RGB display utility. However, users outside of the AWIPS display environment are encouraged to apply this saturation mitigation algorithm as a preprocessing step for the 375-m-resolution $3.9 \mu\text{m}$ channel on VIIRS. This artifact may also be mitigated through user training, as the presence of saturation and radiance fold-over is a strong indication that intense hotspots are present in those pixels. Saturation and radiance fold-over were not found to be a significant issue for ABI and AHI imagery.

5. Summary

In this work, two false color RGB composites were presented that were designed to be useful for the fire weather community. Examples of these RGB composites were created using the operational imagers ABI and AHI on the GEO platform and the operational LEO imager VIIRS, although they may be produced from any imaging instrument with the appropriate spectral channels, as shown in Fig. 2b.

The first, named the Fire Temperature RGB, uses the information at 1.6 , 2.2 , and $3.9 \mu\text{m}$ to relate fire intensity to color in an intuitive manner. According to Wien's displacement law, as fire intensity increases, the peak of the emission spectrum shifts to shorter wavelengths. While a wide variety of hotspots from fires are detectable at $3.9 \mu\text{m}$, a subset of these may be intense enough to be detectable at $2.2 \mu\text{m}$. A further subset of intense active fires may be detectable at $1.6 \mu\text{m}$. This information is conveyed in the imagery as pixels containing hotspots will vary from red to orange to yellow to white on a scale of increasing intensity. These channels, however, are relatively insensitive to smoke. Liquid clouds appear with a blue coloration while ice clouds appear dark green, allowing for the discrimination of cloud phase. While not shown in the examples included here, snow and ice appear black, as they are poorly reflective in any of the three channels. This composite is scaled to provide a similar appearance of hotspots between day and night. However, it is common for fire activity to calm down at night. Based on how the $3.9 \mu\text{m}$ channel is scaled, information on clouds and the surrounding background surface is lost without reflected solar radiation and not all satellite imagers provide data from these three channels at night. Clouds will obscure hotspots and inhibit fire detection any time they are present. However, at night, clouds

are difficult to detect in the Fire Temperature RGB, making it difficult to differentiate changes in fire behavior from changes in sky cover without additional information.

The Fire Temperature RGB is not a quantitative retrieval of the actual fire temperature. This RGB composite simply uses the blackbody emission characteristics of hotspots based on temperature to relate fire intensity to the RGB color space in an intuitive manner. An algorithm for the quantitative retrieval of fire temperature at night has been developed by [Elvidge et al. \(2013\)](#). During the daytime, quantitative retrieval of fire intensity using these spectral channels requires accurate knowledge of surface albedo to separate the radiative emissions of the fire from the background of reflected solar radiation in the 1.6 and 2.2 μm bands.

The second RGB composite, the Day Fire RGB, uses information at 0.64, 0.86, and 3.9 μm to detect hotspots from fires in red, healthy vegetation in green, and smoke in a bluish-gray color. Depending on the scaling used, burn scars will appear in a range from dark brown to reddish-brown, and clouds will appear cyan or blue. This RGB composite is designed for daytime-only use.

In both RGB composites, the utility of the imagery for fire detection is most sensitive to the scaling of the 3.9 μm data based on brightness temperatures. Lowering the maximum and minimum scaling bounds may increase probability of detection at the cost of increasing false alarms. Raising the maximum and minimum scaling bounds may decrease probability of detection while decreasing false alarms. These RGB composites are less sensitive to variations in the scaling of the 3.9 μm data based on solar reflectance or radiance. The solar reflectance retrieval requires additional information from a channel in the 10–11 μm atmospheric window and knowledge of the spectral characteristics of the channel used ([Kidder et al. 2000](#)). Use of solar reflectance at 3.9 μm is not recommended for the Fire Temperature RGB, as the background land surface will generally appear too dark and inhibit possible smoke detection.

Examples of the Fire Temperature RGB presented here, particularly the Starbuck Fire (in a grassland environment) and the East Troublesome Fire (in an alpine forest environment), show that this RGB composite provides valuable information for the fire forecasting and management communities. This RGB provides information on the location of the active fire front, and the change in fire intensity associated with changes in wind speed and direction. Synoptic features such as dry cold fronts (cold fronts not associated with clouds and/or precipitation) may be visible in the imagery. When the images are animated, the speed of both fire fronts and synoptic fronts may be estimated, and this information has been used to provide valuable lead time needed for evacuations to take place. In the case of the Starbuck Fire, the passage of the cold front resulted in a rapid change in fire behavior that could be identified by forecasters using the Fire Temperature RGB. Forecasters at the NWS WFO in Dodge City, Kansas, communicated this information to fire management crews and, in response, these crews were able to take timely, appropriate, and effective action. In the aftermath of this event, the Fire

Temperature RGB was distributed throughout the NWS. In the case of the East Troublesome Fire, operational analysis of the Fire Temperature RGB imagery at the NWS WFO in Boulder, Colorado, led to the discovery that the fire had crossed the Continental Divide, which fire managers were previously unaware of. Aircraft reconnaissance had been suspended due to high winds, and surface visibility was limited by complex terrain and optically thick smoke—factors that did not impact the use of the satellite imagery.

The Day Fire RGB and Fire Temperature RGB produced from VIIRS are used operationally by the Alaska Fire Service throughout their high-latitude domain. In addition to identifying new fire starts, the Day Fire RGB is used to identify different vegetation types surrounding a fire (e.g., forest versus meadow) that may impact fire behavior. The burn scars, which are evident in the imagery, are used to estimate the fire perimeter when aircraft reconnaissance is unavailable. Smoke evident in the imagery is used to estimate winds in the vicinity of the fire as well. The information on vegetation and smoke is not present in current Active Fire products. The intuitive interpretation of both RGB composites has benefited a variety of users within AFS. This satellite imagery has replaced aircraft reconnaissance as the primary source of information on new fires, and is used to inform the allocation of resources used in fire management.

The RGB approach to fire detection has advantages over the quantitative fire detection products. This includes the ability to assess rapidly the full context of the scene in which a fire is situated. These RGB composites allow a user to identify hotspots from fires, burn scars, smoke, and clouds, and easily relate them to other geographic features of interest, which are not present in a simple “fire mask” that only identifies the hotspots themselves. Rapid temporal changes in the environment of a fire may easily be discerned from animating the images, particularly from the GEO satellite platform. A case study by [Lindley et al. \(2020\)](#) demonstrated that visual analysis of 1-min imagery from ABI provided an earlier detection of a new fire start prior to the operational fire detection algorithm applied to ABI. In addition, the RGB composites discussed here have a visual appeal that cannot be matched by the objective fire detections alone, and this imagery is easier to interpret by users that lack a remote sensing background. However, [Fig. 13](#) also shows that RGB composites and quantitative retrievals may be displayed in a common framework and used together to improve fire detection and characterization. The qualitative nature of the imagery cannot replace the quantitative information provided by active fire retrievals, but they may be used in conjunction with each other for the benefits that each provides.

An inherent limitation in the RGB composite approach is the nonuniform sensitivity to color from one image analyst to the next. For example, utilizing the Day Fire RGB for fire detection typically involves identifying red pixels among a background of green pixels. This may not be ideal for image analysts with deuteranopic or protanopic vision, the most common types of color deficiency. Developing similar imagery

products for the benefit of color-insensitive users is a topic of ongoing research.

Acknowledgments. This work was inspired by the EUMETSAT RGB Workshop in 2012, and specifically Renate Brummer, who encouraged the lead author to develop these RGB composites as a result of that meeting. Special thanks go to the Geographic Information Network of Alaska (GINA) at the University of Alaska Fairbanks for delivering these RGB composites to AICC and Alaska Region National Weather Service partners. Special thanks also go to Chad Gravelle (formerly of NWS Operations Proving Ground) for fast-tracking the Fire Temperature RGB into AWIPS. The author would also like to thank the many colleagues, forecasters, and incident meteorologists that have evaluated these RGB composites and provided valuable feedback. This work was supported by the National Oceanic and Atmospheric Administration (NOAA) under Grant NA19OAR4320073. The thoughtful comments and suggestions by the anonymous reviewers are always appreciated. The views, opinions, and findings contained in this article are those of the authors and should not be construed as an official National Oceanic and Atmospheric Administration (NOAA) or U.S. Government position, policy, or decision.

Data availability statement. All ABI and VIIRS data used in this study are available for download from the NOAA Comprehensive Large Array-data Stewardship System (CLASS) website: <https://www.class.noaa.gov>. AHI data used in this study are archived locally at Colorado State University/Cooperative Institute for Research in the Atmosphere and will be made available upon request sent to the corresponding author.

APPENDIX

List of Acronyms

ABI	Advanced Baseline Imager
AFS	Alaska Fire Service
AGRI	Advanced Geostationary Radiation Imager
AHI	Advanced Himawari Imager
AICC	Alaska Interagency Coordination Center
ASTER	Advanced Spaceborne Thermal Emission and Reflection Radiometer
AVHRR	Advanced Very High Resolution Radiometer
AWIPS	Advanced Weather Interactive Processing System
BLM	Bureau of Land Management
CONUS	Contiguous United States
DNR	Department of Natural Resources
FCI	Flexible Combined Imager
FRP	Fire radiative power
GEO	Geostationary
GINA	Geographic Information Network of Alaska
GIS	Geographic information system
JPSS	Joint Polar Satellite System

LEO	Low-Earth orbiting
MERSI-2	Medium Resolution Spectral Imager-2
METImage	Meteorological Imager
MODIS	Moderate Resolution Imaging Spectroradiometer
MSG	Meteosat Second Generation
OSCAR	Observing System Capabilities Analysis and Review Tool
RGB	Red–green–blue
RMNP	Rocky Mountain National Park
SEVIRI	Spinning Enhanced Visible and Infrared Imager
USFS	U.S. Forest Service
VIIRS	Visible Infrared Imaging Radiometer Suite
WFABBA	Wildfire-Automated Biomass Burning Algorithm
WFO	Weather Forecast Office

REFERENCES

- Abatzoglou, J. T., D. E. Rupp, L. W. O'Neill, and M. Sadegh, 2021: Compound extremes drive the western Oregon wildfires of September 2020. *Geophys. Res. Lett.*, **48**, e2021GL092520, <https://doi.org/10.1029/2021GL092520>.
- Ahmadov, R., and Coauthors, 2017: Using VIIRS fire radiative power data to simulate biomass burning emissions, plume rise and smoke transport in a real-time air quality modeling system. *2017 IEEE Int. Geoscience and Remote Sensing Symp.*, Fort Worth, TX, IEEE, 2806–2808, <https://doi.org/10.1109/IGARSS.2017.8127581>.
- Alaska Fire Service, 2022: Alaska Wildland Fire Information Map Series. Accessed 10 June 2022, <https://blm-egis.maps.arcgis.com/apps/MapSeries/index.html?appid=32ec4f34fb234ce58df6b1222a207ef1>.
- Baldrige, A. M., S. J. Hook, C. I. Grove, and G. Rivera, 2009: The ASTER spectral library version 2.0. *Remote Sens. Environ.*, **113**, 711–715, <https://doi.org/10.1016/j.rse.2008.11.007>.
- Berndt, E., N. Elmer, L. Schultz, and A. Molthan, 2018: A methodology to determine recipe adjustments for multispectral composites derived from next-generation advanced satellite imagers. *J. Atmos. Oceanic Technol.*, **35**, 643–664, <https://doi.org/10.1175/JTECH-D-17-0047.1>.
- Bessho, K., and Coauthors, 2016: An introduction to Himawari-8/9—Japan's new-generation geostationary meteorological satellites. *J. Meteor. Soc. Japan*, **94**, 151–183, <https://doi.org/10.2151/jmsj.2016-009>.
- Broomhall, M. A., L. J. Majewski, V. O. Villani, I. F. Grant, and S. D. Miller, 2019: Correcting Himawari-8 Advanced Himawari Imager data for the production of vivid true-color imagery. *J. Atmos. Oceanic Technol.*, **36**, 427–442, <https://doi.org/10.1175/JTECH-D-18-0060.1>.
- CNN, 2017: Wildfires burn more than 1 million acres, taking 7 lives. Accessed 7 September 2022, <https://www.cnn.com/2017/03/07/us/wildfires-texas-deaths/>.
- Colorado Encyclopedia, 2023: East Troublesome Fire. Accessed 2 May 2023, <https://coloradoencyclopedia.org/article/east-troublesome-fire>.
- Csiszar, I., W. Schroeder, L. Giglio, E. Ellicott, K. P. Vadrevu, C. O. Justice, and B. Wind, 2014: Active fires from the Suomi NPP Visible Infrared Imaging Radiometer Suite: Product status and first evaluation results. *J. Geophys. Res. Atmos.*, **119**, 803–816, <https://doi.org/10.1002/2013JD020453>.
- Delamere, J., C. Waigl, and J. Jenkins, 2021: Firewatch: Fire landscapes from air and space. University of Alaska Fairbanks,

- accessed 9 March 2021, <https://www.gi.alaska.edu/events/science-alaska-lecture-series/4254>.
- d'Entremont, R. P., and L. W. Thomason, 1987: Interpreting meteorological satellite images using a color composite technique. *Bull. Amer. Meteor. Soc.*, **68**, 762–768, [https://doi.org/10.1175/1520-0477\(1987\)068<0762:IMSIUA>2.0.CO;2](https://doi.org/10.1175/1520-0477(1987)068<0762:IMSIUA>2.0.CO;2).
- Dozier, J., 1981: A method for satellite identification of surface temperature fields of subpixel resolution. *Remote Sens. Environ.*, **11**, 221–229, [https://doi.org/10.1016/0034-4257\(81\)90021-3](https://doi.org/10.1016/0034-4257(81)90021-3).
- Elvidge, C. D., M. Zhizhin, F.-C. Hsu, and K. E. Baugh, 2013: VIIRS Nightfire: Satellite pyrometry at night. *Remote Sens.*, **5**, 4423–4449, <https://doi.org/10.3390/rs5094423>.
- EUMETSAT, 2009: Best practices for RGB compositing of multispectral imagery. European Organisation for the Exploitation of Meteorological Satellites Doc., 8 pp., https://www-cdn.eumetsat.int/files/2020-04/pdf_using_rgb_best_practices.pdf.
- Flannigan, M. D., and T. H. Vonder Haar, 1986: Forest fire monitoring using NOAA satellite AVHRR. *Can. J. For. Res.*, **16**, 975–982, <https://doi.org/10.1139/x86-171>.
- Gabbert, B., 2017: Three fires near OK-KS burned over 800,000 acres. *Wildfire Today*, 8 March, <https://wildfiretoday.com/2017/03/08/three-fires-near-ok-ks-border-burned-over-800000-acres/>.
- Giglio, L., and J. D. Kendall, 2001: Application of the Dozier retrieval to wildfire characterization: A sensitivity analysis. *Remote Sens. Environ.*, **77**, 34–49, [https://doi.org/10.1016/S0034-4257\(01\)00192-4](https://doi.org/10.1016/S0034-4257(01)00192-4).
- , J. Desloitures, C. O. Justice, and Y. J. Kaufman, 2003: An enhanced contextual fire detection algorithm for MODIS. *Remote Sens. Environ.*, **87**, 273–282, [https://doi.org/10.1016/S0034-4257\(03\)00184-6](https://doi.org/10.1016/S0034-4257(03)00184-6).
- , W. Schroeder, and C. O. Justice, 2016: The Collection 6 MODIS active fire detection algorithm and fire products. *Remote Sens. Environ.*, **178**, 31–41, <https://doi.org/10.1016/j.rse.2016.02.054>.
- Glover, D. M., W. J. Jenkins, and S. C. Doney, 2011: Scientific visualization. *Modeling Methods for Marine Science*, Cambridge University Press, 398 pp.
- Goldberg, M. D., H. Kilcoyne, H. Cikanek, and A. Mehta, 2013: Joint polar satellite system: The United States next generation civilian polar-orbiting environmental satellite system. *J. Geophys. Res. Atmos.*, **118**, 13 463–13 475, <https://doi.org/10.1002/2013JD020389>.
- Gueymard, C. A., D. Meyers, and K. Emery, 2002: Proposed reference irradiance spectra for solar energy systems testing. *Sol. Energy*, **73**, 443–467, [https://doi.org/10.1016/S0038-092X\(03\)00005-7](https://doi.org/10.1016/S0038-092X(03)00005-7).
- Hillger, D. W., and Coauthors, 2013: First-light imagery from Suomi NPP VIIRS. *Bull. Amer. Meteor. Soc.*, **94**, 1019–1029, <https://doi.org/10.1175/BAMS-D-12-00097.1>.
- Ichoku, C. M., R. Kahn, and M. Chin, 2012: Satellite contributions to the quantitative characterization of biomass burning for climate modeling. *Atmos. Res.*, **111**, 1–28, <https://doi.org/10.1016/j.atmosres.2012.03.007>.
- Jin, M., and R. E. Dickinson, 2010: Land surface skin temperature climatology: Benefitting from the strengths of satellite observations. *Environ. Res. Lett.*, **5**, 044004, <https://doi.org/10.1088/1748-9326/5/4/044004>.
- Johnston, J. M., and Coauthors, 2020: Development of the user requirements for the Canadian WildFireSat mission. *Sensors*, **20**, 5081, <https://doi.org/10.3390/s20185081>.
- Judd, D. B., and G. Wysocki, 1975: *Color in Business, Science, and Industry*. 3rd ed. Wiley, 483–486.
- Kaufman, Y. J., R. G. Kleidman, and M. D. King, 1998: SCAR-B fires in the tropics: Properties and remote sensing from EOS-MODIS. *J. Geophys. Res.*, **103**, 31 955–31 968, <https://doi.org/10.1029/98JD02460>.
- Kidder, S. Q., D. W. Hillger, A. J. Mostek, and K. J. Schrab, 2000: Two simple GOES imager products for improved weather analysis and forecasting. *Natl. Wea. Dig.*, **24**, 25–30.
- Lensky, I. M., and D. Rosenfeld, 2008: Clouds-Aerosols-Precipitation Satellite Analysis Tool (CAPSAT). *Atmos. Chem. Phys.*, **8**, 6739–6753, <https://doi.org/10.5194/acp-8-6739-2008>.
- Li, F., X. Zhang, S. Kondragunta, C. C. Schmidt, and C. D. Holmes, 2020: A preliminary evaluation of GOES-16 active fire product using Landsat-8 and VIIRS active fire data and ground-based prescribed fire records. *Remote Sens. Environ.*, **237**, 111600, <https://doi.org/10.1016/j.rse.2019.111600>.
- Lindley, T. T., A. R. Anderson, V. N. Mahale, T. S. Curl, W. E. Line, S. S. Lindstrom, and A. S. Bachmeier, 2016: Wildfire detection notifications for impact-based decision support services in Oklahoma using geostationary Super Rapid Scan satellite imagery. *J. Oper. Meteor.*, **4**, 182–191, <https://doi.org/10.15191/nwajom.2016.0414>.
- , and Coauthors, 2019: Proposed implementation of warn-on-detection fire warnings for public and firefighter safety. *Fifth Conf. on Weather Warnings and Communications*, San Diego, CA, Amer. Meteor. Soc., 4.1., <https://ams.confex.com/ams/47BC5WxComm/meetingapp.cgi/Paper/358595>.
- , and Coauthors, 2020: Ground-based corroboration of GOES-17 fire detection capabilities during ignition of the Kincaid Fire. *J. Oper. Meteor.*, **8**, 105–110, <https://doi.org/10.15191/nwajom.2020.0808>.
- Matson, M., and J. Dozier, 1981: Identification of subresolution high temperature sources using a thermal IR sensor. *Photogramm. Eng. Remote Sens.*, **47**, 1311–1318.
- Meerdink, S. K., S. J. Hook, D. A. Roberts, and E. A. Abbott, 2019: The ECOSTRESS spectral library version 1.0. *Remote Sens. Environ.*, **230**, 111196, <https://doi.org/10.1016/j.rse.2019.05.015>.
- Mildrexler, D. J., M. Zhao, and S. W. Running, 2011: Satellite finds highest land skin temperatures on Earth. *Bull. Amer. Meteor. Soc.*, **92**, 855–860, <https://doi.org/10.1175/2011BAMS3067.1>.
- Miller, S. D., Y.-J. Noh, and A. K. Heidinger, 2014: Liquid-top mixed-phase cloud detection from shortwave-infrared satellite radiometer observations: A physical basis. *J. Geophys. Res. Atmos.*, **119**, 8245–8267, <https://doi.org/10.1002/2013JD021262>.
- , T. J. Schmit, C. J. Seaman, D. T. Lindsey, M. M. Gunshor, R. A. Kohrs, Y. Sumida, and D. Hillger, 2016: A sight for sore eyes: The return of true color imagery to geostationary satellites. *Bull. Amer. Meteor. Soc.*, **97**, 1803–1816, <https://doi.org/10.1175/BAMS-D-15-00154.1>.
- , D. T. Lindsey, C. J. Seaman, and J. E. Solbrig, 2020: GeoColor: A blending technique for satellite imagery. *J. Atmos. Oceanic Technol.*, **37**, 429–448, <https://doi.org/10.1175/JTECH-D-19-0134.1>.
- NWS Boulder, 2020a: “East Troublesome Fire, in Grand county, has rapidly increased in intensity this afternoon on satellite. #Coxw #cofire #EastTroublesomeFire.” Twitter, accessed 12 December 2022, <https://twitter.com/NWSBoulder/status/1319018633570492416>.
- , 2020b: “The East Troublesome Fire, in Grand County, has exploded this afternoon in Fire Imagery. Those in mandatory evacuation areas should evacuate immediately!!! #coxw #cofire #EastTroublesomeFire.” Twitter, accessed 12 December 2022, <https://twitter.com/NWSBoulder/status/1319044505543282689>.

- NWS Training Center, 2017: Using GOES-16 to enhance wildfire IDSS. YouTube, accessed 12 April 2017, <https://www.youtube.com/watch?v=P1oVI9nL9LQ>.
- Prins, E. M., and W. P. Menzel, 1994: Trends in South America biomass burning detected with the GOES visible infrared spin scan radiometer atmospheric sounder from 1983 to 1991. *J. Geophys. Res.*, **99**, 16719–16735, <https://doi.org/10.1029/94JD01208>.
- Raytheon Intelligence and Space, 2022: Advanced Weather Interactive Processing System. Accessed 12 December 2022, <https://www.raytheonintelligenceandspace.com/what-we-do/space-solutions/awips>.
- Roberts, G., M. J. Wooster, G. L. W. Perry, and N. Drake, 2005: Retrieval of biomass combustion rates and totals from fire radiative power observations: Application to southern Africa using geostationary SEVIRI imagery. *J. Geophys. Res.*, **110**, D21111, <https://doi.org/10.1029/2005JD006018>.
- Schmidt, C. C., J. Hoffman, E. Prins, and S. Lindstrom, 2012: GOES-R Advanced Baseline Imager (ABI) algorithm theoretical basis document for fire/hot spot characterization, version 2.5. NOAA/NESDIS/STAR Algorithm Theoretical Basis Doc., 97 pp.
- Schmit, T. J., P. Griffith, M. M. Gunshor, J. M. Daniels, S. J. Goodman, and W. J. Lebar, 2017: A closer look at the ABI on the GOES-R series. *Bull. Amer. Meteor. Soc.*, **98**, 681–698, <https://doi.org/10.1175/BAMS-D-15-00230.1>.
- Schroeder, W., P. Olivia, L. Giglio, and I. A. Csiszar, 2014: The new VIIRS 375-m active fire detection data product: Algorithm description and initial assessment. *Remote Sens. Environ.*, **143**, 85–96, <https://doi.org/10.1016/j.rse.2013.12.008>.
- Sharma, G., and H. J. Trussell, 1997: Digital color imaging. *IEEE Trans. Image Process.*, **6**, 901–932, <https://doi.org/10.1109/83.597268>.
- Skrbek, W., and E. Lorenz, 1998: HSRS—An infrared sensor for hot spot detection. *Proc. SPIE*, **3437**, 167–176, <https://doi.org/10.1117/12.331299>.
- Smith, T., and J. Guild, 1931: The C.I.E. colorimetric standards and their use. *Trans. Opt. Soc.*, **33**, 73–134, <https://doi.org/10.1088/1475-4878/33/3/301>.
- Smith, V. C., and J. Pokorny, 1995: Chromatic-discrimination axes, CRT phosphor spectra, and individual variation in color vision. *J. Opt. Soc. Amer.*, **12**, 27–35, <https://doi.org/10.1364/JOSAA.12.000027>.
- Straka, W., I. Csiszar, S. Kondragunta, C. Seaman, R. Ahmedov, A. Huff, M. Rosenberg, and W. Brewer, 2021: Satellite fire products: More valuable now than ever with longer fire seasons. *2021 IEEE Int. Geoscience and Remote Sensing Symp.*, Brussels, Belgium, IEEE, 699–702, <https://doi.org/10.1109/IGARSS47720.2021.9553725>.
- USFS, 2021: Geospatial data discovery—National USFS Final Fire Perimeter (feature layer). Accessed 17 December 2021, <https://data-usfs.hub.arcgis.com/>.
- von Helmholtz, H., 1924: *Handbuch der Physiologischen Optik*. 3rd ed. Optical Society of America, 480 pp.
- Weaver, J. F., J. F. W. Purdom, and T. L. Schneider, 1995: Observing forest fires with the GOES-8, 3.9- μm imaging channel. *Wea. Forecasting*, **10**, 803–808, [https://doi.org/10.1175/1520-0434\(1995\)010<0803:OFFWTI>2.0.CO;2](https://doi.org/10.1175/1520-0434(1995)010<0803:OFFWTI>2.0.CO;2).
- , D. Lindsey, D. Bikos, C. C. Schmidt, and E. Prins, 2004: Fire detection using GOES rapid scan imagery. *Wea. Forecasting*, **19**, 496–510, [https://doi.org/10.1175/1520-0434\(2004\)019<0496:FDUGRS>2.0.CO;2](https://doi.org/10.1175/1520-0434(2004)019<0496:FDUGRS>2.0.CO;2).
- WMO, 2019: OSCAR: Observing System Capabilities Analysis and Review tool. Accessed 10 September 2019, <https://space.oscar.wmo.int/>.
- Wooster, M. J., B. Zhukov, and D. Oertel, 2003: Fire radiative energy for quantitative study of biomass burning: Derivation from the BIRD experimental satellite and comparison to MODIS fire products. *Remote Sens. Environ.*, **86**, 83–107, [https://doi.org/10.1016/S0034-4257\(03\)00070-1](https://doi.org/10.1016/S0034-4257(03)00070-1).